Geophysical Journal International

Geophys. J. Int. (2014) **197,** 414–434
Advance Access publication 2014 February 10

doi: 10.1093/gji/ggt513

Seismological analyses of the 2010 March 11, Pichilemu, Chile M_w 7.0 and M_w 6.9 coastal intraplate earthquakes

Javier A. Ruiz,[1] Gavin P. Hayes,[2] Daniel Carrizo,[3] Hiroo Kanamori,[4] Anne Socquet[5] and Diana Comte[1,3]

[1] *Department of Geophysics, Faculty of Physical and Mathematical Sciences, University of Chile, Santiago, Chile. E-mail: jruiz@dgf.uchile.cl*
[2] *U.S. Geological Survey National Earthquake Information Center, Golden, CO, USA*
[3] *Advanced Mining Technology Center, Faculty of Physical and Mathematical Sciences, University of Chile, Santiago, Chile*
[4] *Seismological Laboratory, California Institute of Technology, Pasadena, CA, USA*
[5] *ISTerre, UMR 5275 du CNRS, Université Joseph Fourier - Grenoble I, F-38041 Grenoble, France*

Accepted 2013 December 18. Received 2013 October 17; in original form 2013 May 30

SUMMARY

On 2010 March 11, a sequence of large, shallow continental crust earthquakes shook central Chile. Two normal faulting events with magnitudes around M_w 7.0 and M_w 6.9 occurred just 15 min apart, located near the town of Pichilemu. These kinds of large intraplate, inland crustal earthquakes are rare above the Chilean subduction zone, and it is important to better understand their relationship with the 2010 February 27, M_w 8.8, Maule earthquake, which ruptured the adjacent megathrust plate boundary. We present a broad seismological analysis of these earthquakes by using both teleseismic and regional data. We compute seismic moment tensors for both events via a W-phase inversion, and test sensitivities to various inversion parameters in order to assess the stability of the solutions. The first event, at 14 hr 39 min GMT, is well constrained, displaying a fault plane with strike of N145°E, and a preferred dip angle of 55°SW, consistent with the trend of aftershock locations and other published results. Teleseismic finite-fault inversions for this event show a large slip zone along the southern part of the fault, correlating well with the reported spatial density of aftershocks. The second earthquake (14 hr 55 min GMT) appears to have ruptured a fault branching southward from the previous ruptured fault, within the hanging wall of the first event. Modelling seismograms at regional to teleseismic distances ($\Delta > 10^\circ$) is quite challenging because the observed seismic wave fields of both events overlap, increasing apparent complexity for the second earthquake. We perform both point- and extended-source inversions at regional and teleseismic distances, assessing model sensitivities resulting from variations in fault orientation, dimension, and hypocentre location. Results show that the focal mechanism for the second event features a steeper dip angle and a strike rotated slightly clockwise with respect to the previous event. This kind of geological fault configuration, with secondary rupture in the hanging wall of a large normal fault, is commonly observed in extensional geological regimes. We propose that both earthquakes form part of a typical normal fault diverging splay, where the secondary fault connects to the main fault at depth. To ascertain more information on the spatial and temporal details of slip for both events, we gathered near-fault seismological and geodetic data. Through forward modelling of near-fault synthetic seismograms we build a kinematic k^{-2} earthquake source model with spatially distributed slip on the fault that, to first-order, explains both coseismic static displacement GPS vectors and short-period seismometer observations at the closest sites. As expected, the results for the first event agree with the focal mechanism derived from teleseismic modelling, with a magnitude M_w 6.97. Similarly, near-fault modelling for the second event suggests rupture along a normal fault, M_w 6.90, characterized by a steeper dip angle (dip = 74°) and a strike clockwise rotated (strike = 155°) with respect to the previous event.

Key words: Earthquake source observations; Seismicity and tectonics; Continental margins: convergent.

1 INTRODUCTION

On 2010 February 27, a M_w 8.8 megathrust earthquake occurred along the subduction zone in south-central Chile, rupturing the plate interface of the convergent margin between the Nazca and South America plates. The rupture area extended in length over about 450 km (e.g. Lay *et al*. 2010; Vigny *et al*. 2011; Hayes *et al*. 2013), generating a tsunami which propagated across the Pacific Ocean and devastated a broad zone of the Chilean coast. Aftershock activity over the following year has been located (Lange *et al*. 2012; Rietbrock *et al*. 2012; Hayes *et al*. 2013) and, in addition to magnitude and focal mechanism diversity, it has been observed that much of the aftershock seismicity was spatially concentrated in the northern part of the rupture area.

On 2010 March 11, approximately two weeks after and 230 km north of the main shock, a sequence of large, shallow continental crust earthquakes shook Central Chile. Two normal faulting events located near the town of Pichilemu, and with magnitudes M_w 7.0 and 6.9, were separated by just 15 min. The rare occurrence of such large, shallow coastal intraplate events in Chile, and their implications for seismic hazard, motivates further study of these earthquakes in order to understand their relationship to the February 27 main shock.

These two shallow, coastal, intraplate aftershocks at the northern edge of the rupture area of the 2010 Maule mega-thrust earthquake are the first ever instrumentally recorded by local networks among normal faulting events occurring along the Chilean coastal zone. Few shallow crustal recorded earthquakes have occurred along the main Andes Cordillera in Chile; that includes, the 2001, M_w 6.3, Aroma or Chusmiza earthquake (Legrand *et al*. 2007; Farías *et al*. 2010) located in northern Chile, and the 2004, M_w 6.4, Curicó event in south-central Chile (Farías *et al*. 2010). On 2007 April, the seismic crisis of Aysén Fjord, that took place in southern Chile, was characterized by a M_w 6.2 earthquake followed by a local tsunami caused by a triggered landslide (Naranjo *et al*. 2009). Other important shallow crustal events that caused damage during the 20th century include the 1949, M_L 7.5, Punta Arenas earthquake (Lomnitz 1970) along the Magallanes fault near the Froward Cape, and the Las Melosas earthquake, which occurred in the Andes Cordillera near Santiago of Chile in 1958, and has been re-estimated to have a magnitude M_w 6.3 (Alvarado *et al*. 2009).

If one considers the long-term seismic cycle of subduction zones, elastic shortening and subsidence is expected in the crustal forearc region of the overriding plate during the interseismic period of strain accumulation. In contrast, as a result of rapid coseismic strain release during large megathrust ruptures and the subsequent slower deformation of the post-seismic period, relative elastic extension and uplift is likely to occur (e.g. Savage 1983; Hyndman & Wang 1993). Several long-lived tectonic features (faults and folds, both compressional and extensional in nature) have been observed in the upper plate, coastal region above the Chilean subduction zone (e.g. Cortés *et al*. 2012), but the mechanisms responsible for their creation are poorly understood. In addition, prior to the Maule earthquake sequence, no historical crustal seismic activity has been reported in this region. The Pichilemu earthquakes therefore represent the first coincident seismological and geological records of intra(upper) plate coastal faulting, establishing a causal relationship between interplate ruptures and shallow earthquakes, which had only been hypothetically suggested previously (e.g. Delouis *et al*. 1998; Loveless *et al*. 2005, among others). To better understand these events and their role in the seismic cycle of the Chilean mega-thrust, particular attention must be paid to the geometry of the faults involved in these ruptures, and whether they could cause surface-breaking events in the future.

Published InSAR and coseismic GPS static displacement vector observations and modelling show that the Pichilemu earthquakes ruptured two shallow and previously unknown NW/SE-trending faults within the South America Plate (Ryder *et al*. 2012). These authors concluded that the earthquakes did not rupture the N/S-trending Pichilemu-Vichuquen fault.

The source parameters and fault geometry of the first event (14 hr 39 min GMT, hereafter referred to as Event 1) are well constrained. Ryder *et al*. (2012) proposed a fault plane with a strike of N144°E, and a dip angle of 53°, very consistent with the trend of aftershock locations (e.g. Ryder *et al*. 2012). This focal mechanism is also reasonably consistent with the seismic moment tensor computed by the Global Centroid-Moment Tensor (GCMT) group (strike, dip and rake of 144°, 55°, –90° for one nodal plane), and with the U.S. Geological Survey (USGS) W-phase CMT solution (143°, 64°, –89°), which exhibits a slightly higher dip angle. However, solutions for the second event (14h 55 GMT, hereafter referred to as Event 2) show less consistency. The preferred fault plane from Ryder *et al*. (2012) strikes N144°S, with a dip of 60°. On the other hand, GCMT reports a best double-couple characterized by either a very steep plane (159°, 86°, –93°) or a subhorizontal fault (16°, 6°, –53°). A similar discrepancy is observed in the W-phase solution computed by the USGS (nodal plane 1: 166°, 84°, –94°, nodal plane 2: 20°, 7°, –57°). Better constraining the focal mechanism and source parameters of Event 2 using teleseismic recordings is complicated because the observed seismic wave field overlaps with seismic waves radiated by the previous event.

In this study, we analyse teleseismic and regional seismological recordings to better constrain the source parameters and focal mechanisms of both events. We propose point-source and finite-fault source models derived from teleseismic modelling. Regional recordings of both events are analysed to retrieve seismic moment tensors via a W-phase inversion.

Finally, by compiling all these results generated using a variety of seismic wavelengths and frequency bands, we build a kinematic k^{-2} source model with spatially distributed slip over the most plausible fault geometry and extent, which satisfactorily explains additional data from a local short-period network and observed coseismic GPS static displacement vectors at a station installed in the town of Pichilemu.

2 DATA

This section describes the different kinds of seismological data available, spanning regional and teleseismic distances. We also briefly describe the local short-period data used for our forward modelling.

2.1 Seismological recordings data set

Teleseismic broad-band data for both earthquakes were available through the global seismographic network (GSN) and the Incorporated Research Institutions for Seismology (IRIS) Data Management Center. The data set used consists of three component broad-band waveforms that cover distances up to 90° from the source, with a broad azimuthal coverage around the epicentre. The waveform data set was enlarged to include regional recordings from the National Seismological Service (SSN) of the Universidad de Chile (http://www.sismologia.cl/). Fig. 1 shows the broad-band,

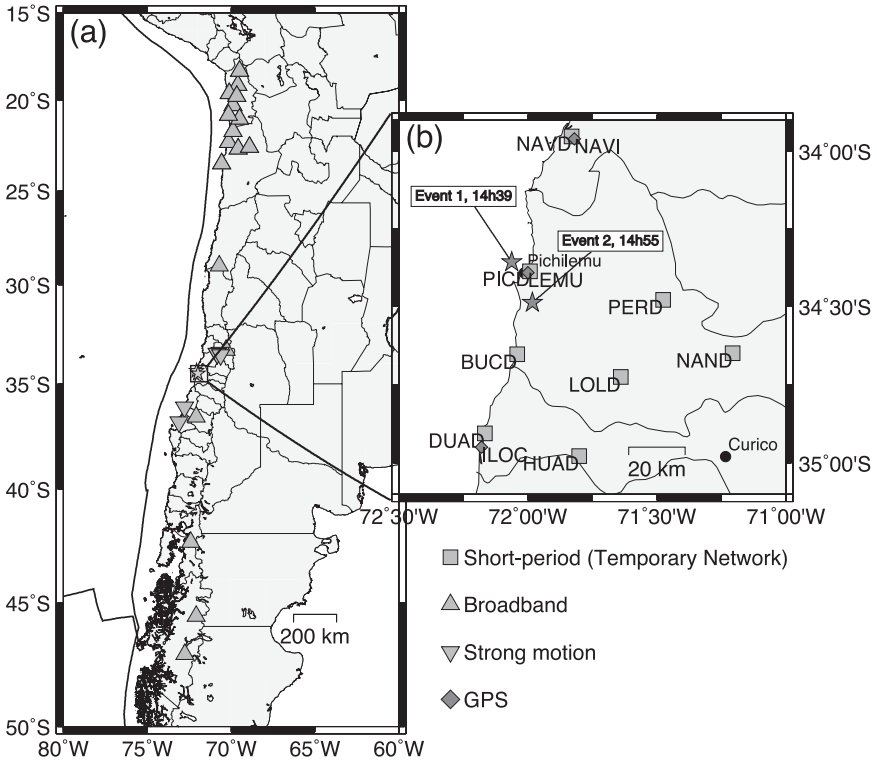

Figure 1. (a) Regional distribution of stations in Chile and (b) enlarged map showing the temporary local short-period network and the hypocentres by Farías *et al*. (2011) of the two studied aftershocks (black star).

regional and local (temporary) station coverage; note that the majority of regional stations are located in central and northern Chile. The northern seismological network is maintained by the SSN in partnership with the Integrated Plate boundary Observatory Chile (IPOC, http://www.ipoc-network.org/) team. Several stations are available in central Chile, mainly around –34.5° latitude near the city of Santiago. Among these are several strong motion and broadband stations that triggered and recorded both events. Fewer receivers are located in southern Chile. Data are also available from a strong motion station in Concepción, ∼300 km to the south of Pichilemu.

2.2 Temporary short-period local network

After the 2010 M_w 8.8, Maule earthquake several seismological stations and temporary networks were deployed over the rupture area, following a huge international community effort for monitoring the aftershock activity in the region, including Chilean, U.K., French, German and U.S. teams. In particular, a rapidly deployed local short-period temporary network recorded both Pichilemu events and a large number of other aftershocks in the weeks following the Maule earthquake (Farías *et al*. 2011). These data are available thanks to the team that installed and operated this network. The station locations are shown in Fig. 1(b); the network covers an area of about one degree squared around the town of Pichilemu. Most of the seismographs were saturated during the strong shaking caused by both events. Nonetheless, it is important to point out that station PICD, located near Pichilemu and close to the two largest aftershock epicentres, did not saturate. In this study, we attempt to exploit these velocity recordings, in particular the closest station to the fault, in order to better constrain the fault geometry and slip distribution for both events.

The three component short-period sensors are I/O SM-6 geophones, with a natural frequency of 4.5 Hz. The instrument amplitude velocity response has a flat transfer function beyond this frequency. Below 4.5 Hz, the amplitude follows a variation of about 40 dB per decade, roughly proportional to $f^{1.5}$, where f is frequency. Two kinds of digitizers were used with a clipping amplitude level of 8.3886×10^6 and 5.767×10^6 Count V^{-1}, respectively.

Fig. 2(a) shows the raw ground-velocity seismograms (three components) of Event 1 recorded at station PICD. The strongest ground motion shaking duration is about 15 s, and the three component data did not saturate. A comparison of signal and seismic noise Fourier spectrum amplitudes shows their ratio is larger than approximately 10^4 in a broad frequency band (Fig. 2b).

As has been pointed out by Havskov (1998) and Aranda (written communication, 2012), some experiments have been conducted in order to compare short-period 4.5 Hz exploration geophones and 1 Hz geophones seismometers at 'an average field site', on the vertical component. The sites tested correspond to a seismic vault in the middle of Bergen City, and a field site on solid rock. These noise studies clearly show that using a 4.5 Hz geophone compared to a 1 Hz geophone will give equal sensitivity for earthquake signals down to 0.2 Hz with systems that have equal gain at 4.5 Hz. If the aim is to record an earthquake signal above 0.2 Hz, the study shows there is little advantage to using a 1 Hz geophone instead a 4.5 Hz sensor. Their study was conducted on instrument corrected signals. Of course, seismic noise and the dynamic range of the sensors have to be taken into account when making this comparison. Unfortunately, for the Pichilemu aftershocks there is no broad-band station located at the same site to enable such a comparison. In fact, there is

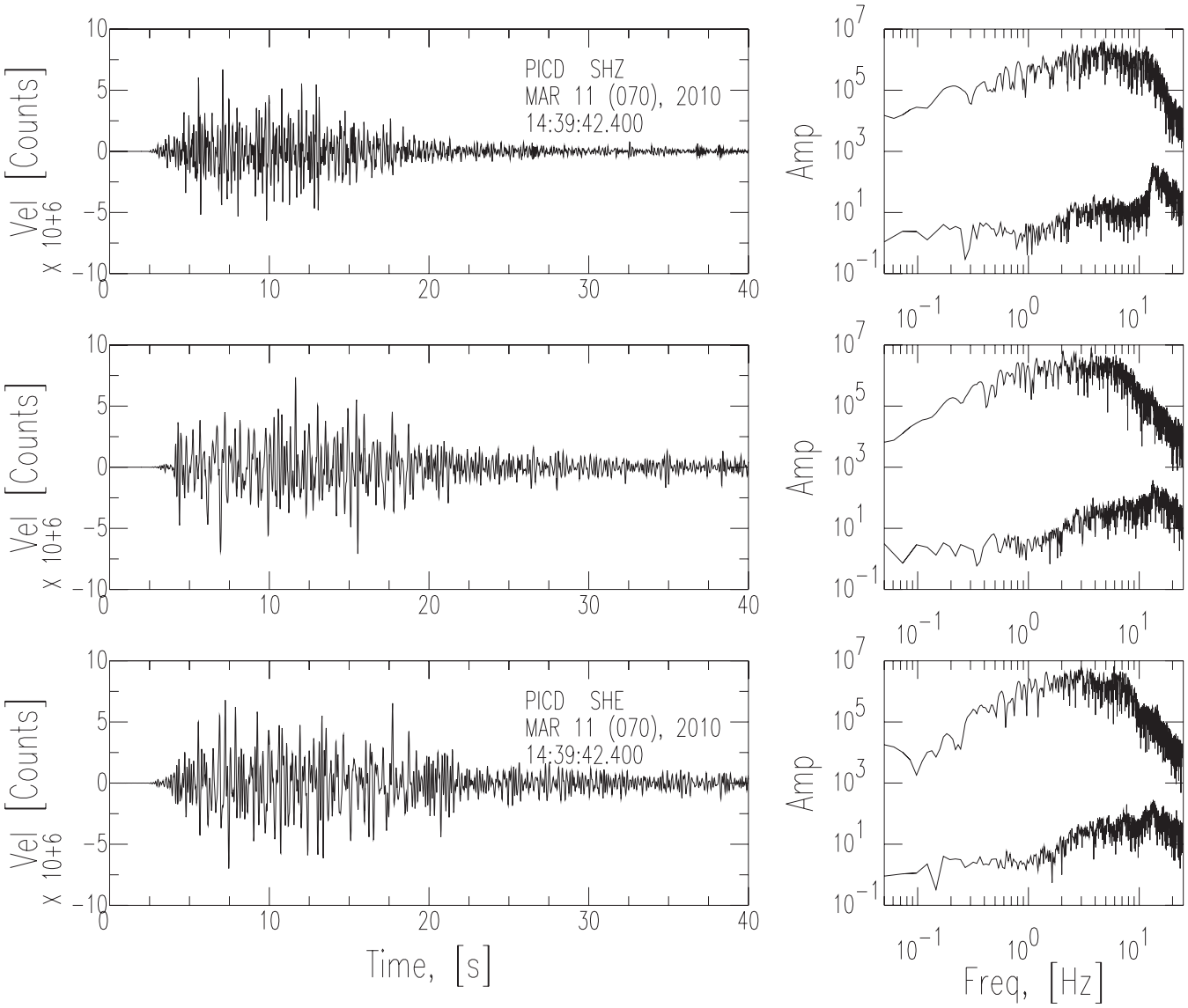

Figure 2. Short-period recording of Event 1 at PICD. Left-hand panel: ground velocity (vertical, north and east components), and right–hand panel: comparison of signal and noise Fourier spectrum amplitudes.

no colocated strong motion or broad-band station near the epicentre of either event. In their absence, in this study we use short-period 4.5 Hz geophones to constrain the source.

Fig. 3 shows an example of frequency domain instrument response deconvolution, using seismic analysis code (SAC, Goldstein *et al*. 2003), applied to the PICD station velocity recording of Event 1. The original and the unfiltered deconvolved ground velocities are shown in Figs 3(a) and (b), respectively, for the vertical component. For comparative purposes the raw seismogram has been multiplied by a scaling factor to correct from counts to physical amplitude. One can note three significant seismic energy arrivals characterized by wavelengths of about 4 s. A very long wavelength signal that contaminates the whole record is also apparent, possibly related to instabilities of the deconvolution process at very low frequencies. The velocity amplitude response transfer function is plotted in Fig. 3(c) where the normalization frequency used is 4.5 Hz. The Fourier spectrum amplitude comparison shows a perfect match for frequencies greater than 4.5 Hz and a factor of 5×10^3 at 0.1 Hz, as one can expect (Fig. 3d). Other stations are located farther than 20 km from Pichilemu, and some components saturated in response to the strong shaking at these sites. Table 1 summarizes the stations and components that did and did not saturate.

2.3 Coseismic GPS static displacements

In addition to the seismological data set, data are available from several continuous GPS (cGPS) sites in Chile. As reported by Ryder *et al*. (2012), the closest cGPS sites to the epicentre of both events are stations LEMU, NAVI and ILOC (Fig. 1b). Station LEMU is particularly interesting because it is located in Pichilemu, so provides valuable information to constrain the source parameters of both events. In this study, we used the coseismic GPS static displacement vectors published by Ryder *et al*. (2012) as a constraint in our analysis (see Table 1, Ryder *et al*. 2012).

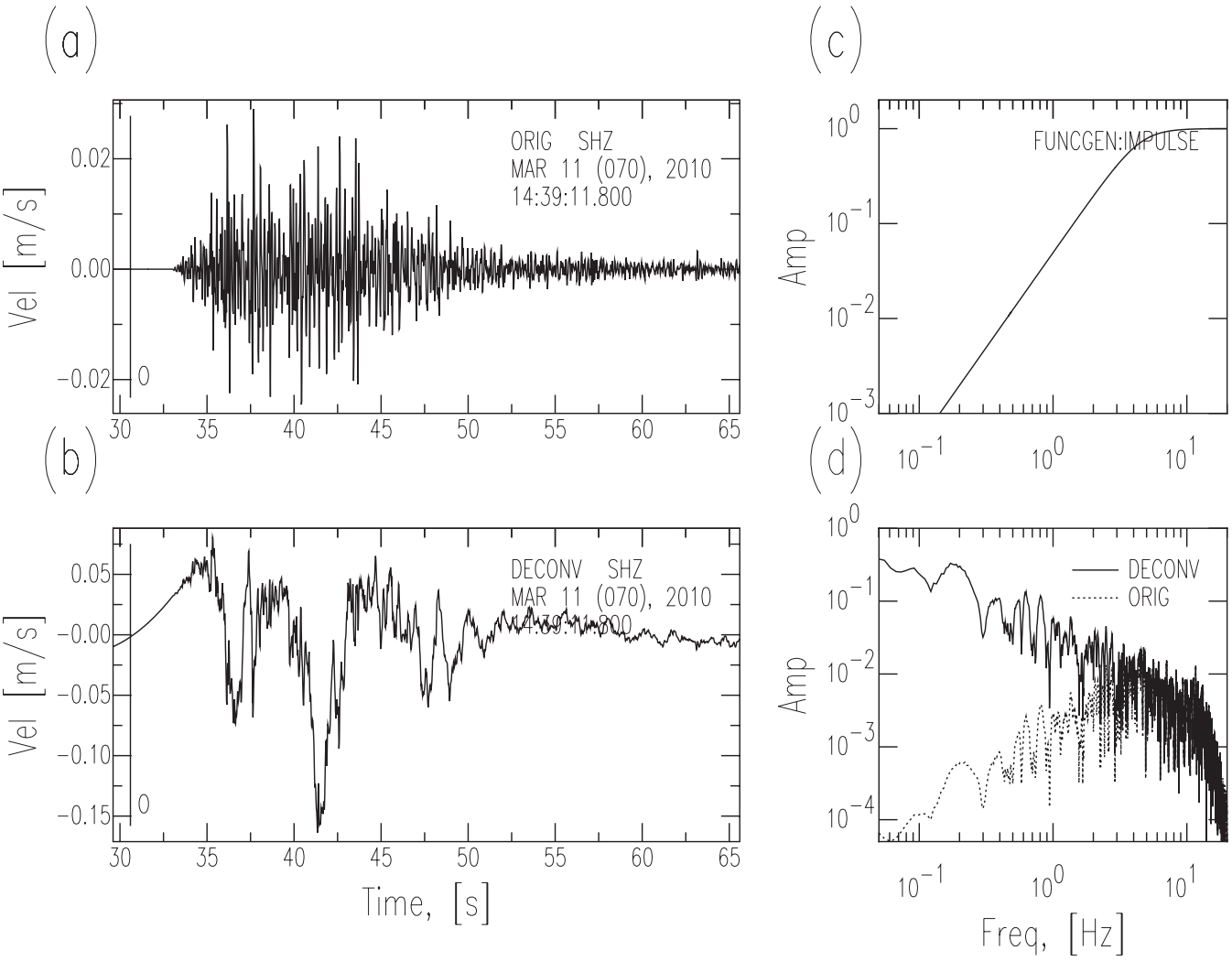

Figure 3. Example of the frequency domain deconvolution applied to the vertical component recording of Event 1, at PICD. (a) Original velocity waveform, (b) unfiltered deconvolved signal, (c) instrument amplitude response, and (d) comparison of the original and deconvolved amplitude Fourier spectrum.

Table 1. Short-period stations list and components that clipped when recording the two aftershocks analysed in this study.

Station	Event 1			Event 2		
	East	North	Up	East	North	Up
BUCD	–	–	–	–	–	–
DUAD	×	×	×	×	×	×
HUAD	×	×	○	○	○	○
LOLD	○	×	○	×	○	○
NAND	○	×	×	×	×	○
NAVD	○	○	○	○	×	○
PERD	×	×	○	×	×	○
PICD	○	○	○	○	○	○

–, None recording available; ×, saturated and ○, not saturated.

As pointed out by Ryder *et al*. (2012), displacement vectors at LEMU and ILOC show a reversed sense of motion for Event 2 with respect to Event 1, though generally with smaller amplitude. Based on these observations, the most likely rupture scenario, proposed by Ryder *et al*. (2012), involves two different normal faults, with the first dipping to the SW and a second, smaller and deeper fault located farther to the SW such that LEMU is in the hanging wall of the first event and the foot wall of the second. Their preferred model uses two parallel faults, the second dipping at a slightly steeper angle compared to the fault associated with Event 1.

3 EARTHQUAKE SOURCE PARAMETERS AND KINEMATIC EARTHQUAKE SOURCE MODELS

The following sections present a broad seismological analysis and kinematic source modelling of both events.

3.1 Earthquake source parameters reported

It is well known that the hypocentral parameters of earthquakes (location and origin time), like all quantitative data estimates, have uncertainties due to different sources of error. Because seismic waves from Event 1 overlap with those radiated by Event 2, the source parameters for the latter event are much harder to constrain. Nonetheless several seismological agencies reported earthquake source parameters as summarized in Table 2.

Table 2. Earthquake source parameters of the two Pichilemu earthquakes reported by different seismological agencies (GCMT, USGS/NEIC and SSN).

	Plane 1 Strike/dip/rake	Plane 2 Strike/dip/rake	Lon	Lat	Depth (km)	M_0 (N m)	M_w	Agency
Event 1	144°/55°/–90°	324°/35°/–90°	–34.54	–72.11	12.9	2.39×10^{19}	6.9	GCMT[a]
Event 2	159°/86°/–93°	16°/6°/–53°	–34.53	–72.13	16.3	3.49×10^{19}	7.0	GCMT[a]
Event 1	143°/64°/–89°	320°/26°/–93°	–34.337	–72.083	14	2.97×10^{19}	6.9	USGS/NEIC[b]
Event 2	166°/84°/–94°	20°/7°/–57°	–34.388	–71.966	24	3.07×10^{19}	6.9	USGS/NEIC[b]
Event 1	–	–	–34.301	–72.129	33	–	–	SSN[c]
Event 2	–	–	–34.451	–72.206	31	–	–	SSN[c]

[a]Centroid location (Ekström *et al*. 2012).
[b]Centroid location and teleseismic W-phase moment tensor solution.
[c]Coordinates correspond to hypocentre location.

The SSN located both earthquakes offshore, at about 30 km depth, with Event 2 located to the south of Event 1 (Fig. 4). In contrast, the hypocentral locations from the USGS National Earthquake Information Center (NEIC) placed Event 1 offshore and Event 2 inland, with shallower hypocentral depths of 14 and 24 km, respectively. Fig. 4 also displays the epicentres determined by Farías *et al*. (2011) using a local short-period network, locating Events 1 and 2 offshore and inland, 8 km NW and 10 km S of Pichilemu, respectively.

GCMT retrieved the centroid location of both events and located them offshore, separated by just 2 km horizontally, with corresponding centroid depths of 13 and 16 km for Events 1 and 2, respectively (Fig. 4). The GCMT solution for Event 1 corresponds to a normal fault with nodal planes of 144°/55°/–90° and 324°/35°/–90° (strike/dip/rake). The nodal planes for the second event are also characterized by normal faulting, with a fault plane dipping either very steeply (159°/86°/–93°), or subhorizontally (016°/06°/–53°). GCMT estimates the seismic moment for Event 1 as 2.39×10^{19} Nm and 3.49×10^{19} Nm for Event 2, corresponding to moment magnitudes of 6.86 and 6.97, respectively. Teleseismic W-phase inversions from the NEIC suggest Event 1 was predominantly normal faulting, with nodal planes of 320°/26°/–93° and 143°/64°/–89°. The seismic moment of 2.97×10^{19} Nm for this event corresponds to a moment magnitude of 6.92. The best double-couple solution for Event 2 describes nodal planes of 020°/07°/–57° and 166°/84°/–94°, and a seismic moment of 3.07×10^{19} Nm (M_w 6.92). The centroid location of Event 1 was 5 km to the SW of Event 2; depths for the two solutions were 14 and 24 km, respectively. The NEIC W-phase solution for Event 2 used a modified time window and bandpass

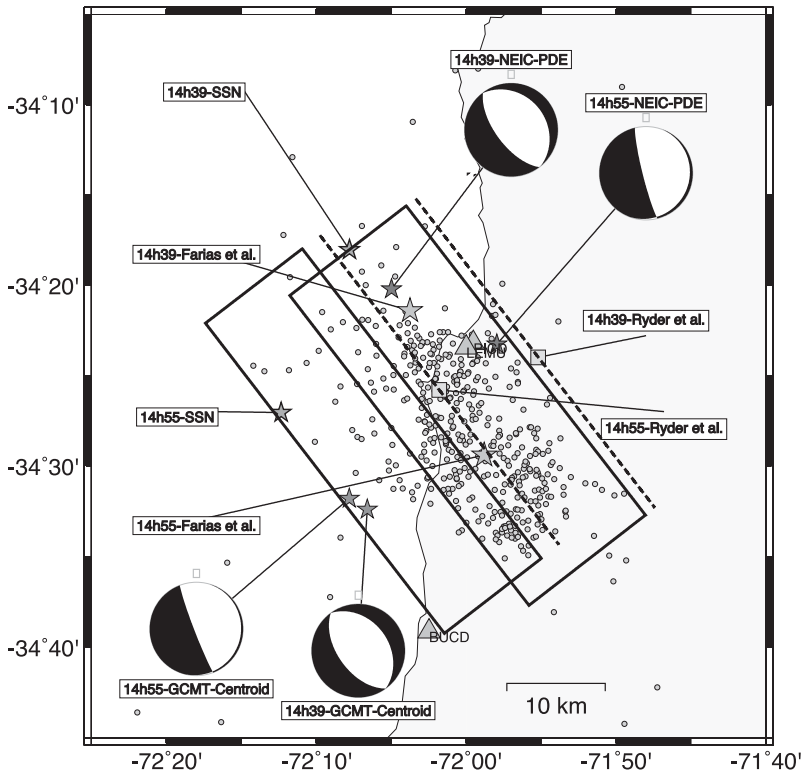

Figure 4. Hypocentre and centroid locations reported by different seismological agencies and published studies. Small rectangles indicate GMT origin times (hour and minute) and the respective seismological agency of reference. Small grey circles show the aftershock seismicity (Farías *et al*. 2011). Grey triangles are local short period stations. Black rectangles correspond to the best fault plane solutions of two events projected to the surface from Ryder *et al*. (2012). Dashed lines are the fault traces.

filter focused on surface waves rather than the traditional W-phase window, to account for the difficulty of inverting noisy data, as discussed in Hayes *et al*. (2009) and Duputel *et al*. (2012).

Overall, the magnitude estimates for Event 1 are quite consistent between seismological agencies, whereas for Event 2 the moment magnitudes vary between agencies and methodologies used to estimate it. This clearly illustrates the difficulty in estimating earthquake source parameters when waveforms are disturbed by a previous earthquake (e.g. Duputel *et al*. 2012). Fig. 4 summarizes the event locations and focal mechanisms. For comparative purposes, the best fault plane solutions of each event proposed by Ryder *et al*. (2012) are also plotted.

3.2 Teleseismic body waves point-source modelling

We first invert broad-band waveforms recorded at teleseismic distances for earthquake source parameters. We first removed instrument from the velocity records by deconvolution, integrated them to ground displacement, and bandpass filtered. We inverted the bandpass filtered teleseismic *P*- and *SH*-wave displacement records to determine the earthquake point-source parameters (strike, dip and rake angles; seismic moment; and source–time function) using an iterative time-domain deconvolution inversion method (Kikuchi & Kanamori 1991). Synthetic Green's functions are computed for distinct source and receiver 1-D crustal velocity models. The inversion technique is based on a least-squares minimization of the difference between the data and synthetic seismograms.

For Event 1, a bandpass filter between 0.005 and 1 Hz is applied to both synthetics and observed data prior to an inversion for the best focal parameters. In this case, 69 vertical and 25 transverse components are used. The focal depth was fixed at 12 km, which was determined with the local short-period network (Farías *et al*. 2011), and four elementary trapezoid source–time functions were used in the inversion. Fig. 5(a) shows the best point-source solution for the focal mechanism and the final source–time function. The total seismic moment retrieved is 1.91×10^{19} Nm, giving a moment magnitude of 6.79. The focal mechanism nodal planes are 143°/52°/–92° and 326°/38°/–87°. The total duration of the source–time function is about 20–25 s, with a large moment rate over the first 10–12 s.

Because Event 2 is much more difficult to model, we carefully established a criterion for the signal to long period noise ratio to search for a good data set of broad-band waveforms. In an attempt to improve data selection, different filter frequency bands were tested to reduce the influence of the seismic waves from Event 1. We tested several frequency bands typically used for inversion of teleseismic body waves (i.e. 0.005–1.0, 0.0075–1.0 and 0.010–1.0 Hz). The criterion used to select the frequency band and stations to be used for inversion of Event 2 was to minimize rms. The upper cut-off frequency does not significantly affect the waveforms, but the lower cut-off frequency allows removal of the very long-period waves originating from Event 1. We found that the frequency band, 0.0075–1 Hz, is preferable because it removes the long-period noise from Event 1, while keeping the important long-period information from Event 2. We applied this bandpass filter to both synthetic and observed seismograms. We selected 44 vertical and 24 transverse components to be used for *P* and *SH* waves, respectively. The focal depth was fixed at 23 km, which was determined with the local network (Farías *et al*. 2011). Two elementary trapezoid source–time functions were used for inversion. Fig. 5(b) shows the best solution for the point-source parameters. The total seismic moment

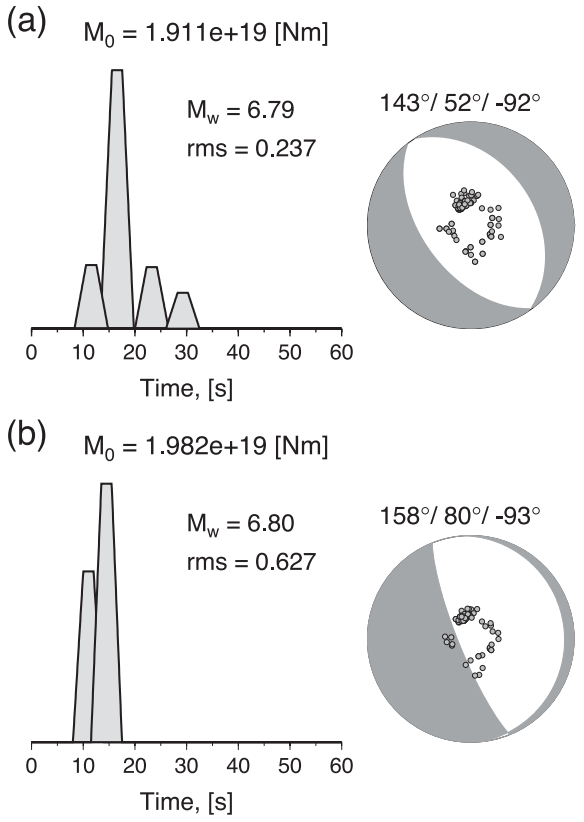

Figure 5. Teleseismic point-source modelling obtained using the Kikuchi & Kanamori (1991) inverse method. Each solution is obtained by jointly inverting *P* and *SH* waveforms, and corresponds to (a) Event 1 and (b) Event 2. The scalar seismic moment, source–time function, RMS value and best double-couple focal mechanism solution are shown.

is 1.98×10^{19} Nm, giving a moment magnitude of 6.80. The focal mechanism nodal planes are 158°/80°/–93° and 353°/11°/–75°. The source–time function has a total duration of about 10 s.

For Event 1, the focal mechanism retrieved by our teleseismic body wave point-source modelling is in good agreement with the best-fitting nodal planes of the moment tensor solutions estimated by GCMT and NEIC. For Event 2, solutions are also in good agreement, though the GCMT and NEIC moment tensors demonstrate a steeper fault plane (a dip angle of 84–86° versus 80° in our analysis), and a slightly greater seismic moment.

3.3 W-phase inversion

The W-phase moment tensor inversion (Kanamori & Rivera 2008) was originally conceived to derive source parameters for very large earthquakes, exploiting the long period content of broad-band seismic recordings (200–1000 s) between the *P* and surface waves. Hayes *et al*. (2009) assessed the performance of this method in real-time and showed that W-phase not only provides rapid and accurate results for large earthquakes, but that this inversion can also be applied successfully to earthquakes as small as $M_w \sim 5.8$ at teleseismic distances. Duputel *et al*. (2011) and Rivera *et al*. (2011) have also been able to demonstrate the application of the inversion at regional distances, exploiting dense networks of stations within 20° of the earthquake, where data are available. Such utility can help the retrieval of source parameters of earthquakes for which data are too noisy at teleseismic distances, as is often the case for events that follow soon after larger shocks (e.g. Duputel *et al*. 2012).

To assess the resolution of the source parameters of the two Pichilemu aftershocks considered in this study, and to supplement the NEIC's teleseismic W-phase solutions described above, the W-phase inversion is applied to retrieve the seismic moment tensor of each event using regional ($\Delta < 12$–20°) broad-band recordings. The determination of moment tensor for Event 1 with regional data is straightforward, because no event preceded it, and the waveforms were not disturbed. A comparison of the regionally and teleseismically derived solutions allows us to asses the quality of the moment tensor solutions of other nearby regional solutions obtained by similarly distributed data. Our best-fitting regional moment tensor for this earthquake (Fig. 6b) yields a normal fault solution, with nodal planes of 326°/18°/–85° and 141°/73°/–92°. These planes are very similar to those derived from the teleseismic W-phase inversion, though the dips of each plane are respectively, 8° shallower and 9° steeper. The seismic moment of 4.41×10^{19} Nm for this event corresponds to a moment magnitude of 7.03, about 50 per cent larger in seismic moment than the teleseismic solution. These differences likely caused by the limited azimuthal coverage of regional data (the azimuthal gap of this regional solution is 250°), and the character of the regional velocity structure in relation to a global average model (e.g. Hayes *et al*. 2013).

For Event 2, we invert for the W-phase moment tensor solution using the same modified time window and filter as those used for the teleseismic inversion, but using only those stations at regional distances. The resulting best double-couple (Fig. 6d) yields nodal planes of 021°/10°/–56° and 166°/82°/–96°, and a seismic moment of 3.35×10^{19} Nm (M_w 6.95). These source parameters are very similar to those recovered teleseismically; more similar in fact than the regional and teleseismic solutions for Event 1. These results give us confidence that despite the noisier data of Event 2, our source parameters are well resolved and Event 2 ruptured a different, much steeper, fault than did Event 1.

3.4 Teleseismic body waves finite-fault source inversion

Next, the source inversion method proposed by Kikuchi & Kanamori (1991) is used to investigate the finite rupture process for these two events using teleseismic body waves, in order to determine the spatial and temporal distribution of coseismic slip on their inferred fault planes. In a similar manner to the teleseismic point-source modelling, synthetic Green's functions were computed using simplified crustal 1-D velocity models at the receiver and source. A time window of 90 s was used for the inversion and the instrument response was removed from the data before applying a time-domain deconvolution inversion approach.

Several inversion tests were performed using different fault dimensions, grid sizes and rupture velocities. For each event, we use the epicentre given by the regional network solution, and the hypocentral depths determined by Farías *et al*. (2011). A minimum RMS criterion was used to search for the best fault plane geometry. In a first set of inversions, models were run while allowing for changes in the fault plane orientation (strike and dip); once a best-fitting geometry was found, a second set of inversions derived our favoured slip distribution. Because both Event 1 and Event 2 are moderate in size, and are imaged using only teleseismic body wave data, we have also performed tests of the grid size for each solution. This allows us to test both the resolvability of short-wavelength features in the spatial distribution of slip, and the stability of the moment rate time function and magnitude estimates. In this kinematic inversion, we assumed that the rupture propagates radially from the hypocentre at a constant rupture velocity.

For Event 1, we jointly invert azimuthally distributed displacement waveforms from teleseismic broad-band stations ($30^\circ < \Delta < 90^\circ$) for 69 vertical *P* waves and 25 *SH* waves. The deconvolved data and synthetics seismograms were bandpass filtered between 0.005 and 1 Hz. The best kinematic inversion was obtained for a fault plane dipping 51° towards the southwest (strike 142°), over a fault plane 45 km × 24 km in size (Fig. 7). The moment-weighted average rake angle over the fault is approximately –98°. This model assumes a rupture velocity of 2.5 km s^{-1}. The total seismic moment is $M_0 = 3.12 \times 10^{19}$ Nm ($M_w = 6.93$).

Fig. 7(a) shows that the fit between observed and synthetic waveforms is good for both *P* and *SH* waves. Observed amplitudes are well modelled, except for noisy stations located on Pacific islands, such as PTCN, TRIS and RAO. The focal mechanism is well constrained by the good azimuthal coverage over the focal sphere, and by the joint inversion of both *P* and *SH* waves. The moment rate time function (Fig. 7c) has a total duration of about 18 s, though the large moment rate is in the first 10 s. The centroid time shift obtained is 9 s. The slip distribution is dominated by one large slip patch in the southeastern region of the fault (with respect to the hypocentre; Fig. 7d), where the maximum slip reaches about 2.5 m. After the inversion tests we performed for different fault geometries, constraining the fault orientation to a dip of about ∼48°, we found that the major slip patch shifted from the top of the fault to a deeper location approximately half of the way along the fault in the dip direction, while the moment rate function remained unchanged. For such a shallow and moderate magnitude earthquake ($M_w \sim 6.5$–7.0), we are likely at the limit of the spatial resolution of this teleseismic inversion technique, particularly for resolving the spatial slip details along dip. To obtain a second independent slip image we used a different teleseismic approach (below). The slip retrieved at the corners of the fault plane is likely an artefact produced by slight misalignments of theoretical and observed *S* waveforms (Fig. 7d).

Event 2 was modelled by jointly inverting 44 vertical *P* waves and 24 *SH* waves, with the distance range and azimuthal coverage similar to Event 1. Because Event 2 occurred just 15 min after Event 1, the teleseismic records are much more difficult to invert. The deconvolved data and synthetics were bandpass filtered between 0.0075 and 1 Hz. Our inversion followed the same procedure outlined above for Event 1. The best kinematic inversion results suggest a steeper fault plane (dip = 78°), rotated slightly clockwise (strike = 155°) with respect to the best geometry of Event 1, and is defined by a rectangular fault of dimensions 45 km × 25 km (Fig. 8). The moment-weighted average rake angle over the fault is –77°. This model assumes a rupture velocity of 2.3 km s^{-1}. The total seismic moment estimated is $M_0 = 2.67 \times 10^{19}$ Nm ($M_w = 6.88$).

Despite the noisier waveforms, the fits between the observed and synthetic *P* waveforms are quite good (Fig. 8a), except for island stations, which exhibit much more complexity (e.g. TAOE, PPTF and ROSA). For some stations, there exists an overlapping signal characterized by a very long wavelength (e.g. CASY, LBTB and NIUE). At DBIC and SUR, one can also notice a baseline offset. We relate these effects to long wavelength seismic waves from Event 1 overlapping the *P* waveforms radiated by Event 2. To reduce their influence on the model, these stations were down-weighted during the inversion. Despite these difficulties, we find that the focal mechanism is well constrained by the good coverage of teleseismic stations over the focal sphere; in particular, XMAS, AFI, PPTF, TAOE, SLBS and NIUE provide strong control on the strike

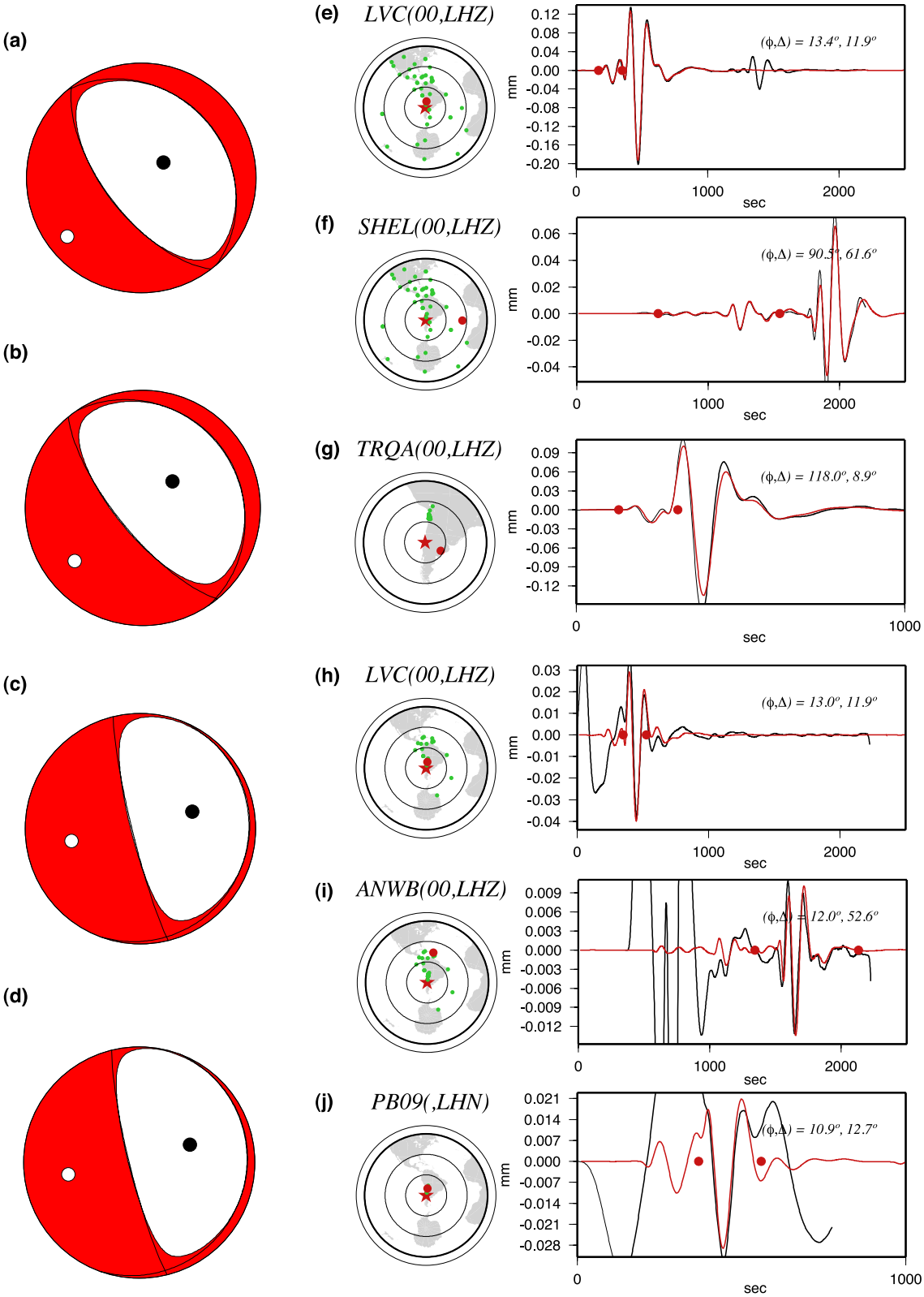

Figure 6. Teleseismic (a, c) and Regional (b, d) W-phase solutions for Event 1 (a, b) and Event 2 (c, d), and examples of waveform fits at representative stations (e–j). Plots (e) and (f) show waveform fits for (a), the teleseismic solution for Event 1; (g) shows a waveform fit for (b), the regional solution for Event 1; (h) and (i) show waveform fits for (c), the teleseismic solution for Event 2; and (j) shows a waveform fit for (d), the regional solution for Event 2.

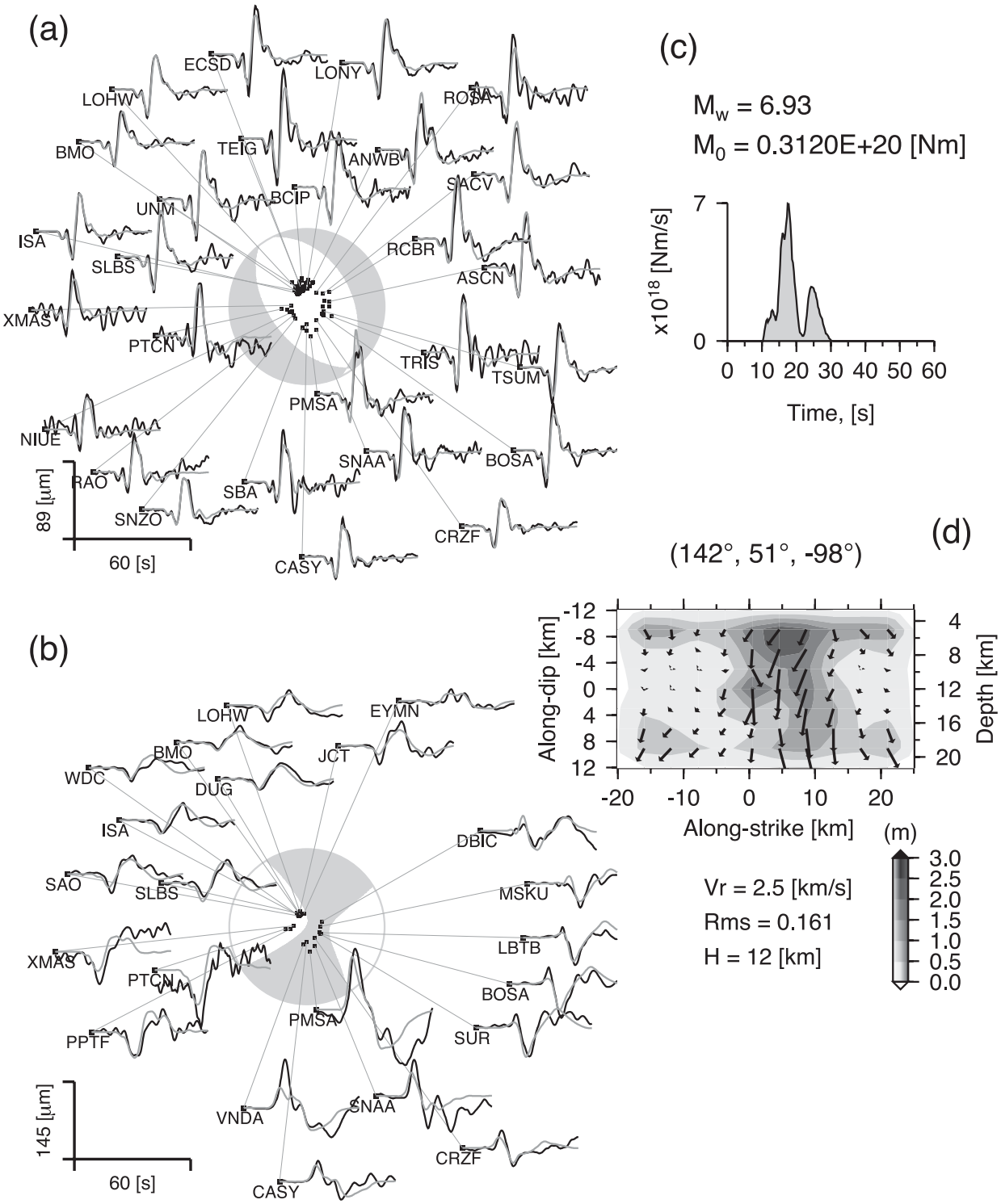

Figure 7. Teleseismic finite source model for Event 1, obtained by jointly inverting *P* and *SH* waveforms. Comparison of observed (black line) and synthetic (grey line) teleseismic waveforms for (a) *P* and (b) *SH* waves. (c) Final slip distribution, moment rate source–time function, and corresponding focal mechanism. The rupture speed was fixed to $V_r = 2.5$ km s^{-1}, and the (0, 0) point along-dip and along-strike directions corresponds to the nucleation location. Arrows represent the slip direction on the fault scaled to slip amplitude.

and dip angles of the vertical fault plane because of their location on the focal sphere. In addition, CASY is a nodal station, evident from the *P*-wave amplitude. After the test to determine fault geometry and orientation, it was clear that *SH*-wave amplitudes are better modelled with a steeper fault plane than when using a shallower one. The *SH* waveforms selected are not affected by the very long wavelength noise (Fig. 8b). This provides high confidence both in the strike and the dip angles of the steeper fault plane. In Fig. 8(b), *SH* waveform fits are compared. Again, the match is good, and only minor amplitude mismatches are observed at LBTB and JUBA.

The moment rate time function for this solution is shown in Fig. 8(c); it has a total duration of about 15 s, though significant

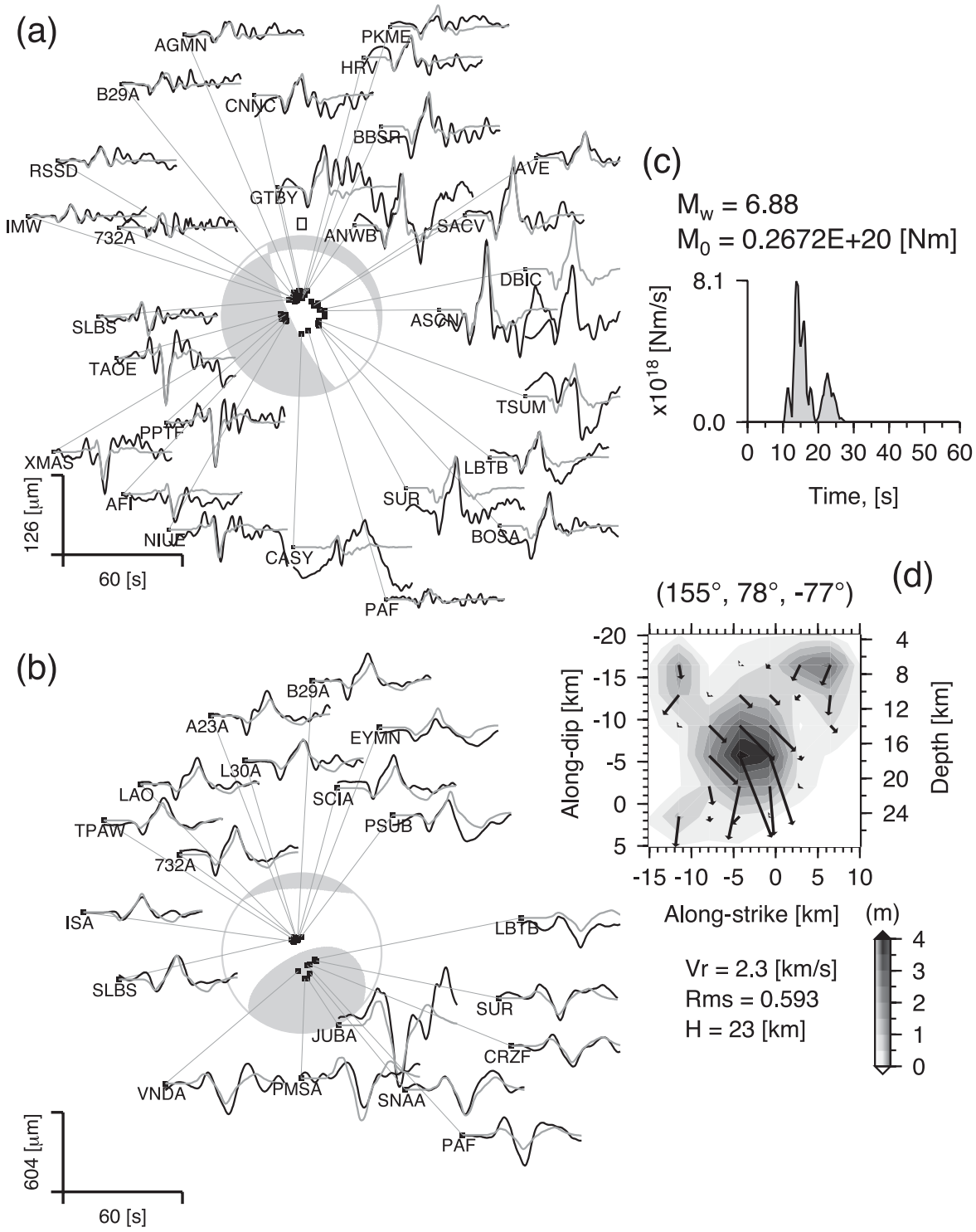

Figure 8. Teleseismic finite source model for Event 2. See Fig. 7 caption for details.

moment rate is in the first 10 s. The centroid time shift obtained is 6.7 s. The slip distribution is dominated by one large circular patch of motion in the northwestern part of the fault (with respect to the hypocentre; Fig. 8d), reaching a maximum offset of about 3.5 m.

To complement and verify slip models obtained by our body wave inversions, we perform a more detailed analysis of the slip distribution for Event 1 following the approach of Ji *et al*. (2002), which uses a wavelet-based approach to invert *P*, *SH*, Rayleigh and Love waves using a variable rupture velocity over an assumed fault plane. We analysed 39 teleseismic broad-band *P* waveforms, 22 broad-band *SH* waveforms and 55-long-period surface waves. Data are chosen to obtain an azimuthally balanced data set, while avoiding the inclusion of data with small signal-to-noise ratios. Body waves are filtered between 0.005 and 1 Hz; surface waves between 0.002 and 0.005 Hz. We use the same regionally defined hypocentre (longitude = –72.06°; latitude = –34.36°; depth = 12 km), and a fault plane from our teleseismic point-source modelling above (strike 145°, dip 55°). The conjugate plane to this solution was also

tested, but was found to not fit the data as well as the chosen fault plane.

Results (Fig. 9) show striking similarity to the body wave only solution (Fig. 7), with slip dominated by a single patch southeast of the hypocentre, reaching approximately 3 m, predominantly at shallow depths. The moment rate function indicates a source duration of around 15 s, with the large moment rate in the first 10 s. Waveform fits (Fig. 9b) are excellent, for both body and surface waves. Over the patch of highest slip, rupture velocity varies between 1.5 and 2.5 km s^{-1}. The total seismic moment is $M_0 = 3.10 \times 10^{19}$ Nm ($M_w = 6.93$), identical to the body wave solution for this event. The similarity between these solutions lends further confidence in our previous results for Event 2, which could not be modelled with this approach due to the complex and noisier nature of the waveforms.

3.5 Near-fault ground motion modelling

This section focuses on building an earthquake source model using a kinematic k^{-2} source approach and a forward modelling strategy, which we will use to compute near-fault ground motions that explain

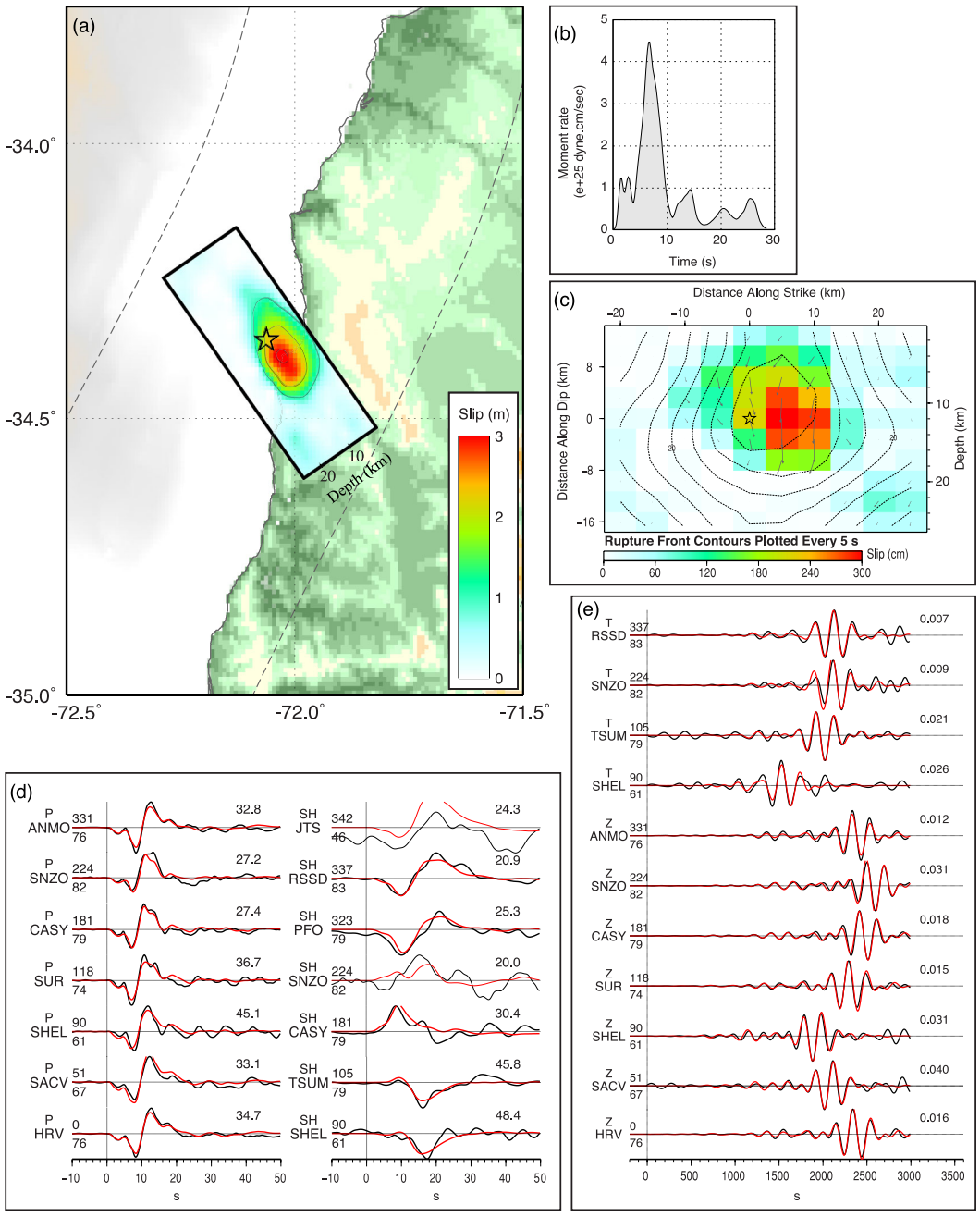

Figure 9. Finite fault solution for Event 1 following the approach of Ji *et al*. (2002). Panel (a) shows a map view representation of the solution, indicating a broad patch of slip reaching approximately 3 m along the shallow fault plane to the southeast of the hypocentre (star). Contours show the depth of the slab from the USGS Slab1.0 model (Hayes *et al*. 2012), in 20 km increments. In (b), the moment rate function for this solution indicates that the majority of moment rate occurred within the first 10 s after origin. Panel (c) shows a fault plane view of the inversion solution. The star indicates the location of the hypocentre, and grey arrows represent the direction of slip in each subfault, scaled by slip. Rupture time contours are plotted every 5 s. Panels (d) and (e) show waveform fits to representative body wave and surface wave records, respectively.

to first-order near-field seismological and geodetic data. The basic approach is to gather all types of data and source models available, such as deconvolved short-period recordings, coseismic static GPS displacements and inverted slip models, and to build a kinematic source model able to explain all of this information.

3.5.1 *Brief description of the kinematic k^{-2} source model*

The near-fault ground motion modelling strategy relies on the basis of the representation theorem of seismic sources (Aki & Richards 1980), which requires a detailed description of the spatial and temporal evolution of the kinematic rupture process on the fault. At close distances comparable with approximately two fault lengths, finite-source effects such as rupture directivity, radiation patterns, and the low-frequency pulse strongly control ground motions.

To model ground motion we follow the approach proposed by Ruiz *et al*. (2007), which is based on a stochastic kinematic k^{-2} source model. The modelling assumes that the rupture front expands radially from the hypocentre at a constant rupture velocity, V_r. The slip distribution is randomly generated by computing a 2-D stochastic spatial random field, and by imposing in the wavenumber domain a k^{-2} spectral decay of the 2-D Fourier amplitudes of slip at high radial wavenumbers (e.g. Andrews 1980; Herrero & Bernard 1994). Andrews (1980) showed that a slip spectrum that decays as k^{-2} in the wavenumber domain radiates far-field displacements that follow the widely observed ω^{-2} spectral decay. The assumption in this model is that the stress drop, $\Delta\sigma$, is scale-invariant. Based on this concept, Herrero & Bernard (1994) introduced the '*k*-squared' model in which the slip spectrum decays as k^{-2} beyond a corner wavenumber, k_c, which is related to a characteristic fault length. The slip velocity functions are set up according to the kinematic k^{-2} source model (Ruiz *et al*. 2007), where a *k*-dependent rise-time is preserved following the approach of Bernard *et al*. (1996). This kinematic rupture model allows us to control the rupture directivity effect in a broad frequency band. Synthetic seismograms are computed by convolving the resulting slip-velocity function at each point on the fault with the respective numerical point-source Green's function of the medium.

Several methods have been proposed to generate spatial random k^{-2} slip distributions (e.g. Herrero & Bernard 1994; Mai & Beroza 2002; Gallovič & Brokešová 2004), but most of these techniques introduce random phases that do not allow control of the exact location of the largest asperities over the fault. In this study, we propose a methodology to built a stochastic k^{-2} slip distribution by controlling the location of elliptical-crack-like slips. We also introduce a random phase at high wavenumbers to generate spatial heterogeneous k^{-2} slip, as described in Appendix A, while preserving the location of the elliptical asperities.

3.5.2 *Modelling ground displacements in the near-fault region*

Here, we exploit data from the nearest stations to the fault, such as the PICD short-period seismometer and the LEMU cGPS station. At PICD, instrument response is deconvolved from short-period velocity recordings and records are integrated into displacement; at LEMU only coseismic static displacements are used. Both stations are located just a couple of kilometres away from the inferred faults, almost directly above both, making the modelling of ground motion very sensitive to finite-source effects and fault geometry. Our aim is to describe long and intermediate characteristic wavelengths of slip; as such, this study focuses on frequencies below 1 Hz.

The complete seismic wave field of Green's functions is computed in a layered medium at each subfault using the AXITRA code (Coutant 1989), which is based on the discrete wave number method (Bouchon & Aki 1977). The 1-D velocity crustal model used is described in Mendoza *et al*. (1994). The numerical scheme implemented on AXITRA allows the computation of Green's functions that capture both the dynamic and static displacement field at the receiver.

To build an earthquake source model we generate random heterogeneous slip distributions and run a kinematic forward model to compute the complete displacement (dynamic and static) wave field at PICD and LEMU. The k^{-2} heterogeneous slip distribution is generated following the methodology described in Appendix A. For each simulation, we compare (1) the observed and synthetic ground displacements at PICD filtered in the passband of 0.15–0.75 Hz, and (2) the observed and modelled coseismic static displacement vector at LEMU.

For Event 1, a rectangular fault plane ($L \times W = 50 \times 25\,\mathrm{km}^2$) was subdivided onto a 128×64 regular grid mesh. The hypocentre was buried at 12 km depth, and the fault plane constrained to strike $= 145^\circ$, dip $= 55^\circ$ and rake $= -90^\circ$, which agrees well with the fault mechanism obtained from teleseismic modelling, teleseismic and regional W-phase inversions, and the best fault plane model from Ryder *et al*. (2012).

One can observe overall similarities in the slip distribution for Event 1 obtained in this study from teleseismic data with that proposed by Ryder *et al*. (2012). For example, the roughly elliptical shape slip imaged by Ryder *et al*. (2012) and the slip distribution (Fig. 9c) obtained with the Ji *et al*. (2002) approach, agrees well in term of spatial distribution, though the details of slip differ at intermediate and short wavelengths. The fault geometry and slip retrieved with jointly inverted *P*, *SH* waves and surface waves (Fig. 9) is used as a reference to construct a kinematic earthquake k^{-2} source model in the near-fault region, because this better explains a larger data set in comparison to other slip models. Instead of using these slip models to compute ground displacements in the near-field, we use them as reference slip distributions to build a heterogeneous k^{-2} slip distribution following the method described in Appendix A. We build the final slip model by summing the contributions from several slip patches on the fault. Four slip patches were tested, where the largest attempts to mimic the ellipse-like slip distribution from Ryder *et al*. (2012) and those derived in this study from teleseismic data. The other three slip patches were located adjacent to the hypocentre—two to the right (southeast), and one to left (northwest)—to mimic the observation of the largest amount of slip being located along the southeast region of the fault. For simplicity, these three patches were defined as roughly circular. Their locations, along strike and dip, were tested after a comparison of the observed and synthetic bandpassed ground displacements at PICD. The relative amplitude of each slip patch was adjusted by hand, in order to match data and synthetics at PICD and LEMU simultaneously. During this process, several random slip distributions were generated and tested. A second set of forward models was subsequently tested by slightly changing the length and width of the patches, and by varying their relative amplitudes. Improvements to the model, resulting from adjusting the shapes of the slip patches, are not as obvious because there are not enough data in the near-field to better constrain the spatial slip distribution with forward modelling, however the location of the largest asperities are consistent in the different testing carried out. The rupture velocity was initially fixed at $V_r = 0.8\ V_s$; subsequently via tuning, the preferred final rupture velocity value was held constant at $2.35\,\mathrm{km\,s}^{-1}$.

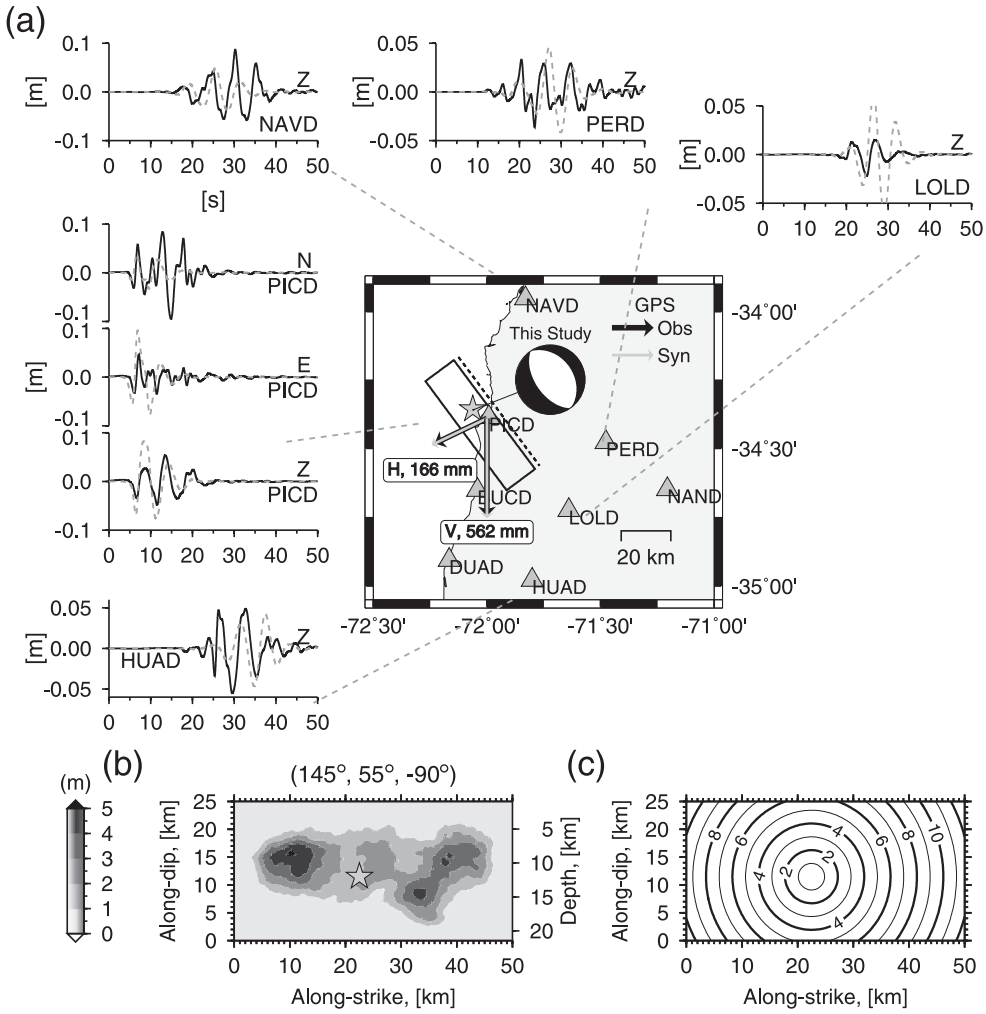

Figure 10. Kinematic k^{-2} finite source model for Event 1. (a) Comparison of synthetic (grey traces) and observed (black traces) ground displacements bandpass filtered between 0.15 and 0.75 Hz. The centre map shows the station locations (grey triangles), and the comparison between the modelled (grey arrow) and observed (black arrow) coseismic static displacement vector for the horizontal and vertical components. (c) The stochastic k^{-2} slip distribution and (c) rupture times contours.

Our favored k^{-2} slip patch model is shown in Fig. 10. Waveform shape and amplitude are fit reasonably well at PICD, on all three components. A strong *S*-wave phase is observed on the north component at approximately 15 s, which was harder to model, and could be associated with a stopping phase. At other stations located farther than 20 km from the source, waveform fits deteriorate, in particular at LOLD (*Z* component). Nonetheless, the observed and modelled coseismic static displacement vectors (horizontal and vertical) match very well at LEMU. The ruptured fault area extent in this model agrees well with the slip distribution obtained teleseismically (Fig. 9c) using the approach of Ji *et al.* (2002), and the overall elliptical-slip-like feature remains quite similar in both slip models. However the k^{-2} kinematic forward modelling introduces intermediate wavelengths of the spatial distribution of slip that are not clear in the slip imaged at teleseismic distances. This is because waveforms recorded in the near-fault region are more sensitive to these intermediate and short wavelengths. The k^{-2} slip distribution also reveals an elliptical-slip-like distribution. Slip is distributed over a rectangular area of dimension, $40 \times 15\,\mathrm{km}^2$. The seismic moment derived from this forward modelling is $M_0 = 3.58 \times 10^{19}$ N·m (M_w 6.97), with an average slip of 1.06 m.

For Event 2, the fault plane dimensions were fixed at $L \times W = 40 \times 25\,\mathrm{km}^2$, following the fault extent inferred from the teleseismic finite-fault inversion (Fig. 8d). This fault was subdivided into a 128×64 regular grid mesh, and the hypocentral depth was fixed at 23 km. Since the fault plane geometry for this event was more difficult to define, we began forward modelling with a focal mechanism set to match the geometry obtained from our best teleseismic finite-fault inversion, 155°/78°/–90° (strike/dip/rake), and adjusted as necessary to match the near-field data.

As an initial estimate of the slip distribution, we imposed a circular patch based on our teleseismic modelling results, with a radius of about 7 km. This patch was located 5 km to left (northwest) and 5 km up dip from the hypocentre. Next, several random slip distributions were tested by slightly adjusting the patch size and its location. Comparisons between synthetics and waveforms/displacement vectors modelled at PICD and LEMU, respectively, show a systematic polarity mismatch on the vertical component. By decreasing the fault dip angle and shifting the hypocentre towards the SW, the polarity of the *Z* component changed, and all three components matched their synthetics much better. Notice that LEMU is located near a nodal plane, so, the vertical static displacement is very sensitive to the inferred dip.

After these minor adjustments of fault geometry and epicentre, the fault mechanism was fixed at 155°/74°/–90°, which is closer to the NEIC W-phase and GCMT solutions than to the shallower fault plane geometry solution proposed by Ryder *et al*. (2012). This adjusted fault mechanism also agrees with our teleseismic finite-fault inversion. Next, we proceeded to improve the slip distribution on the fault. In addition to the largest slip patch defined previously, two additional crack-like slip patches were added, one to the right (southeast), and one to left (northwest) of the hypocentre. For simplicity circular patches were used. Their locations along strike and dip were tested by comparing observed and modelled band-pass filtered ground displacement records at PICD. The relative amplitudes of the slip patches were adjusted by hand; several random slip distributions were generated and tested, and modified in order to simultaneously match data and synthetics at PICD and LEMU.

Waveform data were best fit by locating one of the two small patches of slip in the shallow, northwest corner of the fault plane near the largest slip patch, and the second in the deeper, southwest quadrant near the hypocentre. The horizontal static displacement vector at LEMU was better matched when slip was increased to the left (northwest) side of the hypocentre. The initial rupture velocity was fixed at $V_r = 0.8\ V_s$, but ground displacements at PICD were better matched by decreasing the rupture velocity to a preferred final value of 1.95 km s^{-1}.

Our favoured slip distribution is shown in Fig. 11. Fits between data and synthetics at PICD are quite good, except for the north component where modelled amplitude is too low, though there is still good coherency to the waveforms. The seismograms modelled at LOLD (vertical component) also agree well. The observed and modelled coseismic static displacement vectors (horizontal and vertical components) match quite well at LEMU, though the horizontal component is rotated slightly counter-clockwise with respect to the observation. The ruptured fault area extent in this model agrees well with the slip distribution obtained teleseismically (Fig. 8d) using the approach of Kikuchi & Kanamori (1991), in that the main slip feature is a roughly circular slip patch located up-dip and to left of the hypocentre. As mentioned earlier, the stochastic k^{-2} source model introduces intermediate wavelength to the slip distribution that is not obvious in slip models imaged from teleseismic distances. The slip is distributed over a rectangular area of dimensions 25 × 12 km^2, with a mean value of 0.9 m. The seismic moment derived from this forward modelling is $M_0 = 2.81 \times 10^{19}$ N m (M_w 6.90).

Our results suggest that these two events were similar in size, but it is worth noting that the effective ruptured area of Event 1 was double that of Event 2. This implies that the static stress drop of Event 2 was at least twice as large, though our kinematic k^{-2} source model implies that its rupture velocity was slower. From the standard scaling relation (Kanamori & Anderson 1975), for a given seismic moment, stress drop is proportional to $S^{-1.5}$, thus a factor of 2 difference in S (rupture area) means a factor of approximately 3.0 difference in stress drop.

3.5.3 *Final fault model proposed and geological interpretation*

The preferred final fault plane geometry models are those generated and tested via kinematic k^{-2} earthquake source modelling—Figs 10 and 11 for events 1 and 2, respectively. As pointed out earlier,

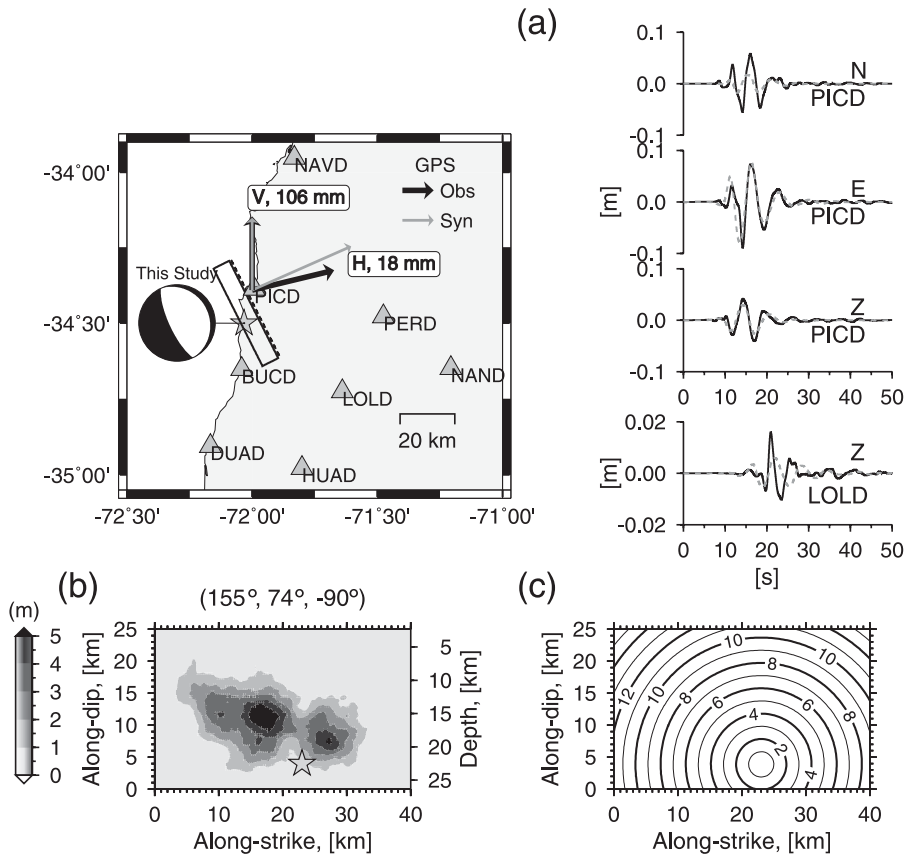

Figure 11. Kinematic k^{-2} finite source model for Event 2. See Fig. 10 caption for details.

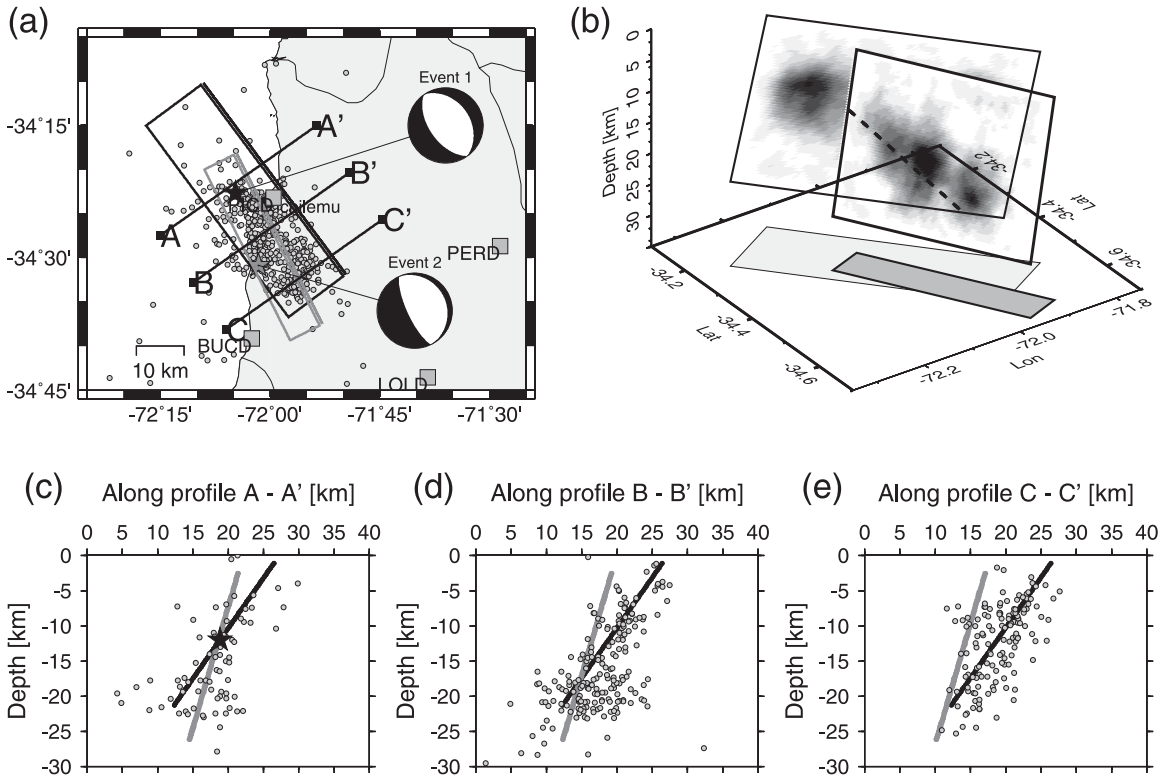

Figure 12. Final fault plane geometry models proposed in this study for the two aftershocks. (a) Map displaying the fault planes projected to the surface (black rectangles) and their respective fault trace (dashed lines). The hypocentres of the local aftershock seismicity are represented by small grey circles. Stations locations (grey squares) and the hypocentre (grey stars) locations linked to their focal mechanisms are also shown. (b) Model and slip distribution of two faults, where the fault splay intersection is shown by the dashed dark line. Comparison of seismicity and fault dipping at depth are displayed along three profiles (c) A–A′, (d) B–B′ and (e) C–C′.

fault geometry and slip extent is similar among all of the solutions derived for Event 1 in this study, as well as with the model proposed by Ryder *et al*. (2012). The preferred fault geometry for Event 2 is has been tuned using data from the near-fault region, which better explain the closest displacements recorded at PICD, and the coseismic static displacement vector at LEMU. This slip model (Fig. 11b) preserves the major long wavelength characteristics of the slip imaged teleseismically using the Kikuchi & Kanamori (1991) approach.

Fig. 12 shows our favoured fault plane geometries for each event. The map view highlights the surface projections of the fault configurations, showing the second fault is rotated clockwise with respect to the first (Fig. 12a). A 3-D view of the two faults model is shown in Fig. 12(b), where we have mapped the fault intersection at depth. Three cross-section profiles are shown perpendicular to the strike of Event 1, to compare the seismicity (Farías *et al*. 2011) recorded over the weeks following these earthquakes to the dipping fault planes of each model (Figs 12c–e). These cross-sections show an agreement between seismicity distributed at depth and the ruptured fault planes. Event 2, with a steeper dip angle, connects with the first fault plane near profile B–B′ at a depth of about 18–20 km. In our favored model (Fig. 11), coseismic slip for Event 2 is distributed in amplitude shallower than 20 km, consistent with this fault plane configuration. The Event 1 structure is oriented N35°W and dips 55° to the SW. The second fault is located in the hanging wall of the first fault, and is oriented N25°W, dipping 74° to the SW. Together these structures form a typical normal fault diverging splay (White *et al*. 1986; Withjack *et al*. 1995; Soliva *et al*. 2008), where the secondary fault (Event 2) is connected to the main fault (Event 1) at depth. We infer from Fig. 12(b) that the peak slip on second fault does not cross the intersection of the two structures, indicating compatible kinematics for both faults—that is, the structures do not significantly offset one another. This kind of extensional fault configuration, with a secondary fault in the hanging wall of a main fault is commonly observed along the Chilean coast (Armijo & Thiele 1990; González *et al*. 2003; González & Carrizo 2003; Allmendinger & González 2010; Cortés *et al*. 2012) and also in other extensional geological environments (e.g. Koledoye *et al*. 2003; Kattenhorn & Pollard 2001; Soliva *et al*. 2008).

Some authors have suggested coastal faults can be loaded and activated almost instantaneously during coseismic earthquake rupture, accommodating trench-orthogonal extension (Delouis *et al*. 1998; Loveless *et al*. 2005; Aron *et al*. 2013). Delouis *et al*. (1998) proposed that the faults are instantaneously loaded (but not necessarily ruptured) during the coseismic rupture of large subduction earthquakes, and partially unloaded in the interseismic period. Others have shown that such coastal faults can also be activated during the interseismic period, accommodating trench-orthogonal shortening (Loveless *et al*. 2005; Farías *et al*. 2011). If one assumes that these faults control long-term coastal uplift, this suggests that a weak fault behaviour is unlikely. Recent palaeoseismological studies of similar coastal faults in northern Chile (Cortés *et al*. 2012) determined that upper plate fault activity (recurrence estimation in the order of 5 ka for M_w 6.5–7.0 intraplate coastal earthquakes) is not in phase with the estimated occurrence of the largest mega-thrust subduction earthquakes (~0.12 ka; Comte & Pardo 1991), and suggest that stress and strain on upper plate faults builds up slowly through several 'cycles' of subduction zone earthquakes.

In light of published geological and tectonic analysis for coastal shallow faulting (e.g. Armijo & Thiele 1990; González & Carrizo 2003; Cortés *et al*. 2012), we hypothesize that the loading mechanism of the upper plate coastal faults in Chile is controlled by the long-term convergence of the subduction zone (over 10^3+ yr). This dominant control is then overprinted by secondary processes such as static and dynamic Coulomb stress changes and fault zone fluid circulation related to large interplate earthquake ruptures. We suspect this model is evidenced by the Pichilemu earthquakes of 2010 March 11; the 2010 February 27, Maule megathrust earthquake positively loaded these intraplate normal faults, triggering their activation during the early post-seismic phase.

4 DISCUSSION AND CONCLUSIONS

We have presented a broad-band seismological analysis of two large aftershocks of the 2010 February 27 Maule earthquake, triggered on 2010 March 11, near the town of Pichilemu, and separated in time by just 15 min. These two shallow crustal earthquakes occurred within the overriding continental South America plate of the Chilean subduction zone margin. We have investigated these earthquakes using both teleseismic and regional data, and via both point-source seismic moment tensor analyses and finite-fault source inversion to better constrain their fault mechanisms and coseismic slip distributions.

The first event, at 14 hr 39 min GMT, ruptured a fault plane striking N145°E, and dipping 55°SW, consistent with the trend of aftershock locations. Teleseismic finite-fault inversions for this event show a large slip zone near the up-dip edge of the fault, also correlating well with the spatial density of aftershocks reported.

Event 2 (14 hr 55 min GMT) appears to have ruptured a fault branching deeper and southward from the fault ruptured by Event 1, within the hanging wall of that first event. Modelling seismograms at regional to teleseismic distances is quite challenging because the observed seismic wavefield of Event 1 overlaps with that of Event 2, increasing apparent complexity for the second event. Results from point- and extended-source inversions at regional and teleseismic distances show that the focal mechanism for the second event features a steeper dip angle (74°) and a strike rotated slightly clockwise (10°) with respect to the previous event. The slip from a teleseismic finite-fault inversion is characterized by a nearly circular slip patch, located slightly northward of and up-dip from the hypocentre.

To gain more insight into the spatial and temporal details of slip for both events, we gathered a variety of near-fault seismological and geodetic data. Through forward modelling of near-fault synthetic seismograms with spatially distributed slip on each fault, we have built kinematic k^{-2} earthquake source models that—to first-order—explain both coseismic static displacement GPS vectors and short-period seismic observations at the closest sites for both earthquakes.

The final preferred fault geometry for Event 1 is a normal fault (rake = –90°), striking 145° and dipping at 55°, as inferred from our teleseismic finite fault modelling. The total seismic moment, $M_0 = 3.58 \times 10^{19}$ N m, implies a magnitude of M_w 6.97. For Event 2, results from near-field modelling agree well with the finite-fault model derived from teleseismic data, and suggest a normal faulting plane (rake = –90°) with a steeper dip angle (dip = 74°) and a strike rotated slightly clockwise (strike = 155°) with respect to Event 1. The seismic moment of $M_0 = 2.81 \times 10^{19}$ N m gives a moment magnitude of M_w 6.90. The static stress drop of Event 2 must be approximately twice as large as for Event 1, because of the relative sizes of the two major slip patches despite their similar moments. Furthermore, the preferred rupture velocity for Event 2 is also much slower.

We support the idea that the loading mechanism of upper plate coastal faults, such as those active in these earthquakes, is mainly controlled by the long-term convergence process of the Chilean subduction zone over cycles of about 10^3 yr. However, the high static Coulomb stress change generated by the 2010, M_w 8.8, Maule earthquake at the northern end of the rupture area likely triggered these events earlier than they would have otherwise occurred (Farías *et al*. 2011). These earthquakes may also be influenced by fluid flow along the fault system, as a consequence of accommodating the changes to the regional stress–strain field, potentially an additional mechanism to drive the nucleation of these events. The fault plane of Event 2 is buried to a depth of ∼20–25 km, likely connecting with the seismogenic contact zone of the Nazca and South America plates (see Fig. 3, Farías *et al*. 2011). Fluids are present along the subduction channel located at the plate interface (Contreras-Reyes *et al*. 2010), and can flow upwards into the fractured zone and the Pichilemu fault system. Farías *et al*. (2011) argued that the rupture area coincides with a zone of high V_p/V_s ratio, suggesting weakness in the fault and the presence of fluids. To our knowledge, there is no evidence of fluid flow related to triggering these earthquakes, though fluids and related fluid pressure variations can modify shear stress and friction over the fault, creating the conditions necessary to trigger these earthquakes. We suspect that Event 2 maybe triggered as a consequence of dynamic stress transfer from Event 1 and fluid circulation along the fault system. However, such a hypothesis requires further work to be verified. The fault associated with Event 2 is interpreted as a branch of a primary fault (Event 1), and is connected to the main fault at depth, where both structures form a typical normal fault diverging splay.

Both events provide evidence that significant earthquakes may occur on faults without any evidence of historical activity after large- or mega-thrust earthquakes in subduction zones. Thus, from a seismic hazard perspective, it is important to consider this type of upper plate aftershock activity.

ACKNOWLEDGEMENTS

Some figures were drawn with the software package Generic Mapping Tools (GMT) v4.5 (Wessel & Smith 1998). Signal processing and some figures were done using SAC (Goldstein *et al*. 2003). We thank Carlos Aranda for discussion about SM-6 4.5 Hz geophones and instrument response. We thank Dr Luis Rivera for help provided on some W-phase inversions test done. We thank Dr Bertrand Delouis and one anonymous scientist for their helpful review and comments that helped us to improve the original manuscript. We are grateful to Editor for comments and advice. This study was funded by the Chilean National Science Foundation, FONDECYT Iniciación grant number 11100134.

REFERENCES

Aki, K. & Richards, P.G., 1980. *Quantitative Seismology Theory and Methods,* Vol. 2, W. H. Freeman & Co.

Allmendinger, R.W. & González, G., 2010. Neogene to quaternary tectonics of the coastal Cordillera, northern Chile, *Tectonophysics,* **495**(1–2), 93–110.

Alvarado, P., Barrientos, S., Saez, M., Astroza, M. & Beck, S., 2009. Source study and tectonic implications of the historic 1958 Las Melosas crustal earthquake, Chile, compared to earthquake damage, *Phys. Earth planet. Inter.,* **175**(1–2), 26–36.

Anderson, J.G. & Richards, P.G., 1975. Comparison of strong ground motion from several dislocation models, *Geophys. J. R. astr. Soc.,* **42,** 347–373.

Andrews, D.J., 1980. A stochastic fault model I, static case, *J. geophys. Res.,* **85,** 3867–3877.

Armijo, R. & Thiele, R., 1990. Active faulting in northern Chile: ramp stacking and lateral decoupling along a subduction plate boundary?, *Earth planet. Sci. Lett.,* **98,** 40–61.

Aron, F., Allmendinger, R.W., Cembrano, J., González, G. & Yañez, G., 2013. Permanent fore-arc extension and seismic segmentation: insights from the 2010 Maule earthquake, Chile, *J. geophys. Res. Solid Earth,* **118,** doi:10.1029/2012JB009339.

Bernard, P., Herrero, A. & Berge-Thierry, C., 1996. Modeling directivity of heterogeneous earthquake ruptures, *Bull. seism. Soc. Am.,* **86,** 1149–1160.

Bouchon, M. & Aki, K., 1977. Discrete wavenumber representation of seismic-sources wave fields, *Bull. seism. Soc. Am.,* **67,** 259–277.

Burridge, R. & Willis, J.R., 1969. The self-similar problem of the expanding elliptical crack in an anisotropic solid, *Proc. Cambridge Phil. Soc.,* **66,** 443–468.

Comte, D. & Pardo, M., 1991. Reappraisal of great historical earthquakes in the northern Chile and southern Peru seismic gaps, *Nat. Haz.,* **4,** 23–44.

Contreras-Reyes, E., Flueh, E.R. & Grevemeyer, I., 2010. Tectonic control on sediment accretion and subduction off south central Chile: implications for coseismic rupture processes of the 1960 and 2010 megathrust earthquakes, *Tectonics,* **29,** TC6018, doi: 10.1029/2010TC002734.

Coutant, O., 1989. Programme de Simulation Numérique AXITRA. Rapport LGIT, Université Joseph Fourier, Grenoble, France.

Cortés, A.J., González, G.L., Binnie, S.A., Robinson, R., Freeman, S.P.H.T. & Vargas, G.E., 2012. Paleoseismology of the Mejillones Fault, northern Chile: insights from cosmogenic ^{10}Be and optically stimulated luminescence determinations, *Tectonics,* **31,** TC2017, doi:10.1029/2011TC002877.

Dahlen, F.A., 1974. On the ratio of P-wave to S-wave corner frequencies for shallow earthquake sources, *Bull. seism. Soc. Am.,* **64**(4), 1159–1180.

Delouis, B., Philip, H., Dorbath, L. & Cisternas, A., 1998. Recent crustal deformation in the Antofagasta region (northern Chile) and the subduction process, *Geophys. J. Int.,* **132,** 302–338.

Duputel, Z., Rivera, L., Kanamori, H., Hayes, G.P., Hirsorn, B. & Weinstein, S., 2011. Real-time W phase inversions during the 2011 Tohoku-oki earthquake, *Earth, Planets Space,* **63**(7), 535–539.

Duputel, Z., Rivera, L., Kanamori, H. & Hayes, G., 2012. W-phase fast source inversion for moderate to large earthquakes (1990–2010), *Geophys. J. Int.,* **189**(2), 1125–1147.

Ekström, G., Nettles, M. & Dziewoński, A.M., 2012. The global CMT project 2004–2010: centroid-moment tensors for 13,017 earthquakes, *Phys. Earth planet. Inter.,* **200–201,** 1–9.

Erdèlyi, A., 1954. *Tables of Integral Transforms,* Vol. I, McGraw-Hill Book Company.

Eshelby, J.D., 1957. The determination of the elastic field of a ellipsoidal inclusion and related problems, *Proc. R. Soc. Lond., A* **241,** 376–396.

Farías, M., Comte, D., Charrier, R., Martinod, J., David, C., Tassara, A., Tapia, F. & Fock, A., 2010. Crustal-scale structural architecture in central Chile based on seismicity and surface geology: implications for Andean mountain building, *Tectonics,* **29**(3), TC3006, doi:10.1029/2009TC002480.

Farías, M., Comte, D., Roecker, S., Carrizo, D. & Pardo, M., 2011. Crustal extensional faulting triggered by the 2010 Chilean earthquake: the Pichilemu seismic sequence, *Tectonics,* **30,** TC6010, doi:10.1029/2011TC002888.

Gallovič, F. & Brokešová, J., 2004. On strong ground motion synthesis with k^{-2} slip distributions, *J. Seismol.,* **8,** 211–224.

Goldstein, P., Dodge, D., Firpo, M. & Minner, L., 2003. SAC2000: signal processing and analysis tools for seismologists and engineers, in *IASPEI International Handbook of Earthquake and Engineering Seismology,* eds Lee, W.H.K., Kanamori, H., Jennings, P.C. & Kisslinger, C., Academic Press, Part B, pp. 1613–1614.

González, G. & Carrizo, D., 2003. Segmentación, cinemática y cronología relativa de la deformación tardía de la Falla Salar del Carmen, Sistema de Fallas de Atacama, Cordillera de la Costa de Antofagasta, *Revista Geológica de Chile.* **30**(2), 223–244.

González, G., Cembrano, J., Carrizo, D., Macci, A. & Schneider, H., 2003. The link between forearc tectonics and Pliocene–Quaternary deformation of the Coastal Cordillera, northern Chile, *J. South Am. Earth Sci.,* **16,** 321–342.

Havskov, J., 1998. Preliminary tests of the GeoSys GBV seismic recorder using a 4.5 Hz geophone, Internal report, pp. 1–13.

Hayes, G.P., Rivera, L. & Kanamori, H., 2009. Source inversion of the W-phase: realtime implementation and extension to low magnitudes, *Seismol. Res. Lett.* **80**(5), 817–822.

Hayes, G.P., Wald, D.J. & Johnson, R.L., 2012. Slab1.0: a three-dimensional model of global subduction zone geometries, *J. geophys. Res.,* **117,** B01302, doi:10.1029/2011JB008524.

Hayes, G.P., Bergman, E., Johnson, K.L., Benz, H.M., Brown, L. & Meltzer, A., 2013. Seismotectonic framework of the February 27, 2010 M_w 8.8 Maule, Chile earthquake sequence, *Geophys. J. Int.,* **195,** 1034–1051, doi:10.1093/gji/ggt238.

Herrero, A. & Bernard, P., 1994. A kinematic self-similar rupture process for earthquakes, *Bull. seism. Soc. Am.,* **84**(4), 1216–1228.

Hyndman, R.D. & Wang, K., 1993. Thermal constraints on the zone of major thrust earthquake failure: the Cascadia Subduction Zone, *J. geophys. Res.,* **98**(B2), 2039–2060.

Ji, C., Wald, D.J. & Helmberger, D.V., 2002. Source description of the 1999 Hector Mine, California earthquake. Part I: wavelet domain inversion theory and resolution analysis, *Bull. seism. Soc. Am.,* **92**(4), 1192–1207.

Kanamori, H. & Anderson, D.L., 1975. Theoretical basis of some empirical relations in seismology, *Bull. seism. Soc. Am.,* **65**(5), 1073–1095.

Kanamori, H. & Rivera, L., 2008. Source inversion of W phase: speeding up tsunami warning, *Geophys. J. Int.,* **175,** 222–238.

Kattenhorn, S.A. & Pollard, D.D., 2001. Integrated 3-D seismic data, field analogs and mechanical models in the analysis of segmented normal faults in the with farm oil field, southern England, United Kingdom, *AAPG Bull.,* **85**(7), 1183–1210.

Kikuchi, M. & Kanamori, H., 1991. Inversion of complex body waves, III, *Bull. seism. Soc. Am.,* **81,** 2335–2350.

Koledoye, B., Aydin, A. & May, E., 2003. A new, process-based methodology for analysis of shale smear along normal faults in the Niger Delta, *AAPG Bull., Spec. Fault Seal Issue,* **85,** 445–463.

Kostrov, B.V., 1964. Self-similar problems of propagation of shear cracks, *J. appl. Math. Mech. (PMM),* **28,** 1077–1087.

Lange, D. *et al.*, 2012. Aftershock seismicity of the 27 February 2010 M_w 8.8 maule earthquake rupture zone, *Earth planet. Sci. Lett.,* **317–318C,** 413–425.

Lay, T., Ammon, C.J., Kanamori, H., Koper, K.D., Sufri, O. & Hutko, A.R., 2010. Teleseismic inversion for rupture process of the 27 February 2010 Chile (M_w 8.8) earthquake, *Geophys. Res. Lett.,* **37,** L13301, doi:10.1029/2010GL043379.

Legrand, D., Delouis, B., Dorbath, L., David, C., Campos, J., Marquez, L., Thompson, J. & Comte, D., 2007. Source parameters of the $M_w = 6.3$ Aroma crustal earthquake of July 24, 2001 (northern Chile), and its aftershock sequence, *J. S. Am. Earth Sci.,* **24**(1), 58–68.

Loveless, J.P., Hoke, G.D., Allmendinger, R.W., González, G., Isacks, B.L. & Carrizo, D.A., 2005. Pervasive cracking of the northern Chilean Coastal Cordillera: new evidence for forearc extension, *Geology,* **33**(12), 973–976.

Lomnitz, C., 1970. Major earthquakes and tsunamis in Chile during the period 1535 to 1955, *Geol. Rund.* **59,** 938–960.

Mai, P.M. & Beroza, G.C., 2002. A spatial random field model to characterize complexity in earthquake slip, *J. geophys. Res.,* **107**(B11), 2308, doi:10.1029/2001JB000588.

Mendoza, C., Hartzell, S. & Monfret, T., 1994. Wide-band analysis of the 3 March 1985 central Chile earthquake: overall source process and rupture history, *Bull. seism. Soc. Am.,* **84,** 269–283.

Naranjo, J.A., Arenas, M., Clavero, J. & Muñoz, O., 2009. Mass movement-induced tsunamis: main effects during the Patagonian Fjordland seismic crisis in Aisén (45°25'S), Chile, *Andean Geol.,* **36**(1), 137–145.

Richards, P., 1973. The dynamic field of a growing plane elliptical shear crack, *Int. J. Solids Struct.,* **9,** 843–861.

Rietbrock, A., Ryder, I., Hayes, G., Haberland, C., Comte, D., Roecker, S. & Lyon-Caen, H., 2012. Aftershock seismicity of the 2010 Maule M_w = 8.8, Chile, earthquake: correlation between co-seismic slip models and aftershock distribution?, *Geophys. Res. Lett.,* **39,** L08310, doi:10.1029/2012GL051308.

Rivera, L., Kanamori, H. & Duputel, Z., 2011. W-phase source inversion using the high-rate regional GPS data of the 2011 Tohoku-oki earthquake, *Am. Geophys. Un.,* Abstract G33C-04.

Ruiz, J.A., Baumont, D., Bernard, P. & Berge-Thierry, C., 2007. New approach in the kinematic k^{-2} source model for generating physical slip velocity functions, *Geophys. J. Int.,* **171,** 739–754.

Ryder, I., Rietbrock, A., Kelson, K., Burgmann, R., Floyd, M., Socquet, A., Vigny, C. & Carrizo, D., 2012. Large extensional aftershocks in the continental forearc triggered by the 2010 Maule earthquake, Chile, *Geophys. J. Int.,* Vol. 188, Issue 3, doi: 10.1111/j.1365–246X.2011.05321.x.

Savage, J.C., 1983. A dislocation model of strain accumulation and release at a subduction zone, *J. geophys. Res.,* **88,** 4984–4996.

Soliva, R., Benedicto, A., Schultz, R.A., Maerten, L. & Micarelli, L., 2008. Displacement and interaction of normal fault segments branched at depth: implications for fault growth and potential earthquake rupture size, *J. Struct. Geol.,* **30,** 1288–1299.

Vigny, C. *et al.*, 2011. The 2010 M_w 8.8 maule megathrust earthquake of central Chile, monitored by GPS, *Science,* **332,** 1417, doi:10.1126/science.1204132.

Wessel, P. & Smith, W.H.F., 1998. New, improved version of Generic Mapping Tools released, *EOS, Trans. Am. geophys. Un.,* **79**(47), 579.

White, N.J., Jackson, J.A. & McKenzie, D.P., 1986. The relationship between the geometry of normal faults and that of the sedimentary layers in their hanging walls, *J. Struct. Geol.,* **8**(8), 897–909.

Withjack, A.O., Islam, Q.T. & La Pointe, P.R., 1995. Normal faults and their hanging-wall deformation: an experimental study, *Am. Assoc. Petrol. Geol. Bull.,* **79**(1), 1–18.

APPENDIX A: A SIMPLE WAY TO GENERATE k^{-2} SLIP DISTRIBUTIONS

A.1 Some background on basic source slip functions

We present a simple method to generate random k^{-2} heterogeneous slip distributions. Let us start introducing the well-known circular static crack-type slip solution obtained by Eshelby (1957),

$$\Delta u(r) = \frac{24}{7\pi}\frac{\Delta\sigma}{\mu}\sqrt{a^2 - r^2}, \quad r < a, \tag{A1}$$

where $\Delta\sigma$ is the static stress drop, a is the radius of the crack and μ the rigidity of the medium. This expression can be used straightforward to generate a crack-type slip distribution.

Dahlen (1974) built-up a source model based on the use of three-dimensional dynamical shear fracture solutions (Kostrov 1964; Burridge & Willis 1969; Richards 1973). The initial nucleation is assumed to be self-similar and the rupture front spreads out uniformly from its centre preserving an elliptical shape. For $t > 0$, the extent of the ruptured area is given by $x^2/u^2 + y^2/v^2 \leq t^2$, where u and v are the velocities of crack propagation along the x and y directions. In the self-similar problem, after the passage of the crack tip the shear traction drops instantaneously an uniform stress, $\Delta\sigma$, for all points inside the crack.

Following the work by Burridge & Willis (1969), Dahlen (1974) obtained an exact solution to this dynamic fracture problem by guessing the form of the resulting slip, $\Delta u(x, y, t)$, and then verifying that the guessed form leaded to an uniform stress drop on the fracture surface. The space-time slip function $\Delta u(x, y, t)$ is,

$$\Delta u(x, y, t) = A\sqrt{t^2 - \frac{x^2}{u^2} - \frac{y^2}{v^2}}\, H\left(t - \sqrt{\frac{x^2}{u^2} + \frac{y^2}{v^2}}\right), \tag{A2}$$

where $H(\cdot)$ is the Heaviside step function. The constant A contains most of the complexity of the dynamic problem and it has been shown to be proportional to the stress drop $\Delta\sigma$ through the relationship,

$$A = C\left(\frac{u}{\beta}, \frac{v}{\beta}, \frac{\alpha}{\beta}\right)\frac{\Delta\sigma}{\mu}\beta, \tag{A3}$$

where α and β denote the P- and S-wave velocities, respectively. $C(\cdot)$ is a dimensionless function given in the work by Burridge & Willis (1969) through a complicated expression. In absence of either friction or cohesion, the elliptical self-similar crack grows at a speed $u = c_R$ and $v = \beta$, being c_R the Rayleigh-wave velocity (Burridge & Willis 1969; Richards 1973). These values can thus be taken as upper bounds for the velocities at nucleation. A difficulty with this source model is that it eventually grows to an infinite size. In this study, we are mostly interested in defining a static slip function having some physical basis, thus the mechanism that controls the rupture to stop will not be discussed here.

After Dahlen (1974), the exact self-similar solution (A2) is used for the initiation of the rupture, which will grow in a self-similar manner and will terminate abruptly at a prescribed elliptical shape barrier. Anderson & Richards (1975), for instance, introduced a $t_{\max}$ parameter to define the rupture stopping time, in our description the barrier is simply defined by its semi-major and -minor axis a and b, respectively. Then, the rupture time $t_{\max}$ and the barrier must to verify,

$$t_{\max}^2 = \frac{a^2}{u^2} + \frac{b^2}{v^2}. \tag{A4}$$

When the rupture stops, one get the final 2-D elliptical slip function defined by,

$$\Delta u(x, y) = C\frac{\Delta\sigma}{\mu}\beta\sqrt{t_{\max}^2 - \frac{x^2}{u^2} - \frac{y^2}{v^2}} \quad \text{for } t_{\max}^2 \geq \frac{x^2}{u^2} + \frac{y^2}{v^2}. \tag{A5}$$

A.2 Spectral characteristic of an elliptical crack-type slip

We focus on describing the spectral characteristics of the slip function eq. (A5) on the wavenumber domain, by computing its 2-D Fourier transform. If a function $\eta(x, y)$ is defined as,

$$\eta(x, y) = \left(1 - \frac{x^2}{a^2} - \frac{y^2}{b^2}\right)^{\nu - 1} H\left(1 - \frac{x^2}{a^2} - \frac{y^2}{b^2}\right), \tag{A6}$$

using Fourier transform formulas (8) and (50) by Erdèlyi (1954) (table 1.3 and 1.13, respectively), its 2-D Fourier Transform $\tilde{\eta}(k_x, k_y)$ is,

$$\tilde{\eta}(k_x, k_y) = \pi ab 2^{\nu}\Gamma(\nu)\frac{J_{\nu}(k)}{k^{\nu}}, \quad \mathrm{Re}(\nu) > -1, \tag{A7}$$

where $\Gamma(\cdot)$ is the Gamma function, $J_{\nu}(\cdot)$ is the cylindrical Bessel function of first kind and order ν, and the radial wavenumber is defined as $k = \sqrt{a^2k_x^2 + b^2k_y^2}$.

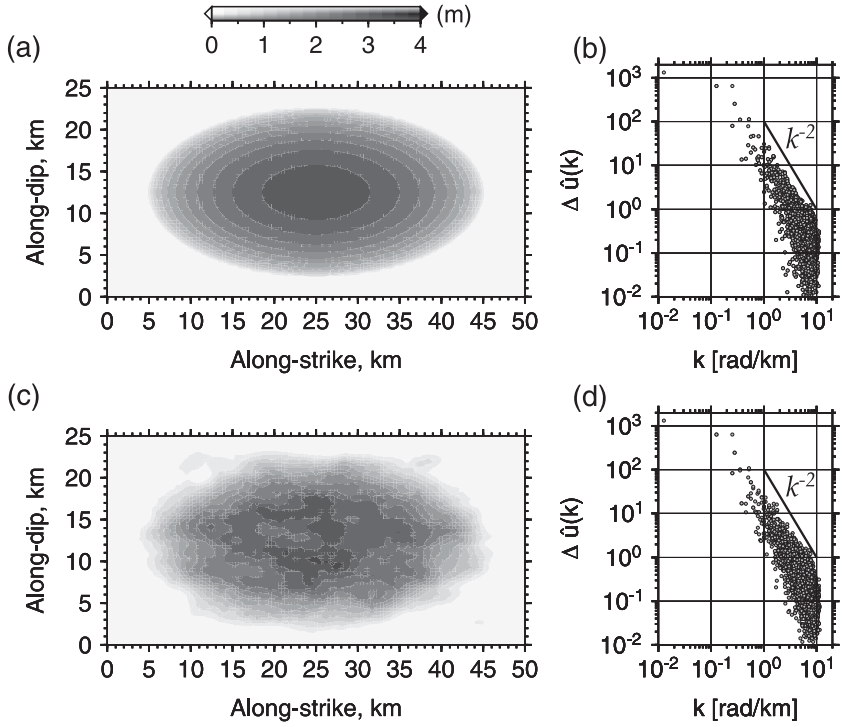

Figure A1. Example of a stochastic numerical generation of a k^{-2} slip distribution using a single elliptical crack-type slip. Original coherent slip with their corresponding (a) spatial and (b) spectral Fourier amplitude representations. Stochastic k^{-2} slip, (c) spatial distribution and (d) spectral Fourier amplitude.

Now it is straightforward to compute the 2-D Fourier transform of eq. (A5) by using eqs (A6) and (A7), with $\nu = 3/2$,

$$\Delta\tilde{u}(k_x, k_y) = C\frac{\Delta\sigma}{\mu}\beta\, t_{\max}^3 u\, v\, \pi\sqrt{2\pi}\frac{J_{3/2}(k)}{k^{3/2}}, \tag{A8}$$

where in this case the radial wavenumber k is defined as, $k = t_{\max}\sqrt{u^2k_x^2 + v^2k_y^2}$. Notice that the constants, $t_{\max}$, u and v are simply scaling factors of the wavenumber components, k_x and k_y. Using asymptotic expressions of cylindrical Bessel function of first kind, one can study the asymptotic spectral behaviour of $\Delta\tilde{u}$ for small and large values of k. Let us examine when $k \to 0$, in this case one get,

$$\Delta\tilde{u}(k_x, k_y) \propto C\frac{\Delta\sigma}{\mu}\beta\, t_{\max}^3\frac{2\pi}{3}u\, v, \tag{A9}$$

that is to say, a constant value. Whereas for large values of k, the 2-D Fourier spectrum of the slip behaves as,

$$\Delta\tilde{u}(k_x, k_y) \propto C\frac{\Delta\sigma}{\mu}\beta\, t_{\max}^3\, \pi\, u\, v\frac{1}{k^2} \propto \frac{1}{k^2}, \tag{A10}$$

so, the spectral amplitude of the slip at high wavenumber is proportional to k^{-2}.

Eq. (A8) can be used directly to generate a stochastic spatial random field for the slip. Notice that the spectral phase is zero for all wavenumbers, so, introducing a random phase for $k > k_c$, in the wavenumber domain, one can built-up a heterogeneous spatial slip based on eq. (A8) by performing the inverse 2-D Fourier transform. The corner radial wavenumber, k_c, is associated with some correlation wavelength, λ_c, through the relation $k_c = 2\pi/\lambda_c$.

From a practical point of view, is more useful to look for a minimum set of parameters to define a slip distribution, so, further approximations and additional hypotheses can be made in order to simplify the description of the slip. Dahlen (1974), following Kostrov (1964) results, gives a simplified expression for the constant C under the assumption of an initial nucleation that is roughly circular, $u \approx v$, a Poisson solid and $u \ll \beta$. The constant is approximately,

$$C \approx \frac{24}{7\pi}\frac{u}{\beta}. \tag{A11}$$

At the elliptical barrier, u, v, a, b and $t_{\max}$, verify, $a = t_{\max}u$, $b = t_{\max}v$, then substituting these parameters and C in eq. (A5) one finally gets,

$$\Delta u(x, y) = \frac{24}{7\pi}\frac{\Delta\sigma}{\mu}a\sqrt{1 - \frac{x^2}{a^2} - \frac{y^2}{b^2}} \quad \text{for } 1 \geq \frac{x^2}{a^2} + \frac{y^2}{b^2}. \tag{A12}$$

A.3 Numerical realization of a k^{-2} slip distribution

In practice, the random slip is constructed over a rectangular fault plane subdivided onto a regular grid mesh. The first stage consists of defining the semi-major and semi-minor axis of an elliptical slip function (eq. A5) and the parameters that lead to defining the maximum slip amplitude at the centre of the elliptical crack. Then, it can be located at any point over the fault plane. The function (A5) is used to construct a discrete slip function over the whole fault. Fig. A1(a) shows an example of a single elliptical crack of dimensions, $a = 20$ km, $b = 5$ km and with a maximum slip of 4.5 m, which is located over a rectangular fault plane ($L \times W = 50 \times 25\,\text{km}^2$). The amplitude of the 2-D Fourier transform of the slip is shown in Fig. A1(b), note the spectral amplitude decay at high wavenumber that falls off as k^{-2}.

To generate a stochastic random spatial slip while preserving a roughly a coherent elliptical shape, a discrete 2-D Fourier transform is applied. A correlation wavelength is defined, in this case $\lambda_c = 10$ km, and a random phase is introduced for all $k > k_c$,

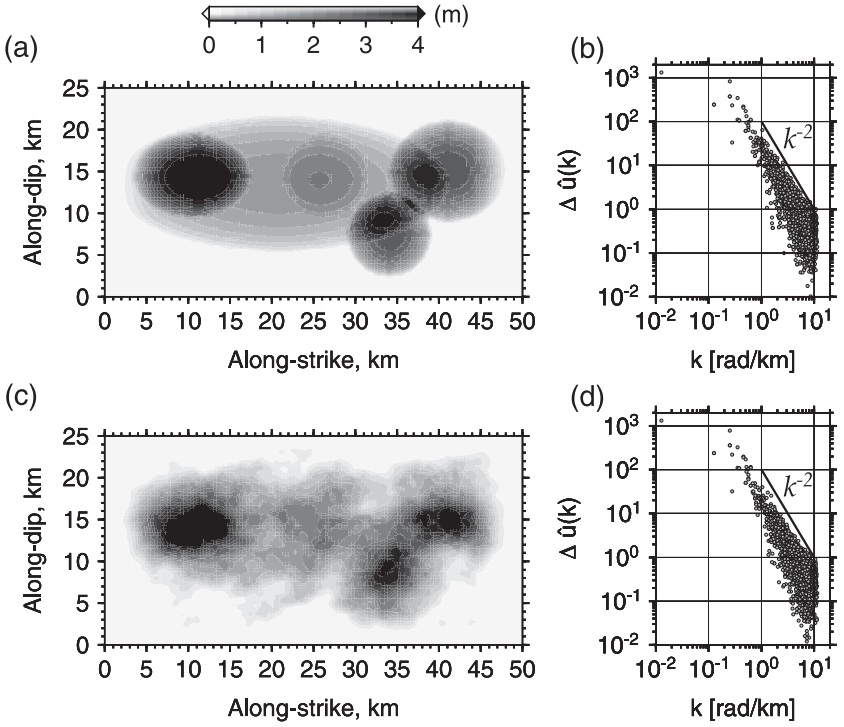

Figure A2. Example of a stochastic numerical generation of a k^{-2} slip distribution composed of five different elliptical crack-type slip. Original coherent slip with their corresponding (a) spatial and (b) spectral Fourier amplitude representations. Stochastic k^{-2} slip, (c) spatial distribution and (d) spectral Fourier amplitude.

otherwise, the phase is kept unchanged. The inverse 2-D Fourier transformation is performed, after imposing in the wavenumber domain the constraint,

$$\Delta\tilde{u}(k_x, k_y) = \Delta\tilde{u}^*(-k_x, -k_y), \tag{A13}$$

where the asterisk denotes complex conjugate, so that the inverse transform would be real. Because the phase is random for high wavenumber, the final slip would have small negative values, thus a positivity criterion is applied by setting to zero negative values of the slip, as well as a tapering window function at the ends of the fault plane. Afterwards, the final slip is renormalized to the final seismic moment. Fig. A1(c) shows a random spatial heterogeneous slip realization of the original one (Fig. A1a). Notice that overall the elliptical shape is preserved, but the random phases introduce heterogeneities at intermediate and short wavelengths. Fig. A1(d) displays the spectral amplitude of the 2-D Fourier transform of the random slip.

The same methodology can be applied by defining several elliptical crack-type slip over the fault in order to locate asperities at some specific locations on the fault plane. An example is shown in Fig. A2, where five elliptical crack-type slips are located on the fault at different locations.